Nonadiabatic molecular dynamics simulation of photodissociation and geminate recombination of I_2 liquid xenon

V. S. Batista and D. F. Coker
Department of Chemistry, Boston University, 590 Commonwealth Avenue, Boston, Massachusetts 02215

(Received 14 December 1995; accepted 29 May 1996)

In this paper we investigate the *B* state predissociation and subsequent geminate recombination of photoexcited iodine in liquid xenon using a coupled quantum-classical molecular dynamics method and a model Hamiltonian gained from the diatomics-in-molecules semiempirical approach to excited state electronic structure including spin-orbit coupling. We explore the capabilities of these techniques as applied to studying the dynamics of realistic condensed phase reactions by comparing with available experimental data from recent ultrafast spectroscopic studies and Raman scattering measurements. We present a microscopic understanding of how the solvent perturbs the electronic states of the chromophore and opens various channels for dissociation from the bound excited *B* state. We survey the different possible dissociative channels and determine their relative importance as a function of solvent density. We find that predissociation usually occurs during the first bond extension within about 50–100 fs. We follow our trajectories out to 2 ps and observe early solvent collisions which, at the highest solvent densities studied, often result in geminate recombination to the excited bound A' state with in this time. © *1996 American Institute of Physics.* [S0021-9606(96)03133-9]

I. INTRODUCTION

The photodissociation and geminate recombination of I_2 in solution is regarded as the paradigm for excited state condensed phase chemical reactions and has been studied extensively, both experimentally and theoretically. Much of the earlier work in this area is summarized in the excellent review article by Harris *et al.*[1] The experiment involves photoexcitation from the ground *X* state of I_2 to below the dissociation threshold of its excited bound *B* state, rapid electronically nonadiabatic relaxation to some dissociative state, then further nonadiabatic motion involving solvent caging of the dissociating fragments and recombination on various possible bound state surfaces followed by vibrational relaxation.

In this paper, we focus on the first two picoseconds of dynamics after photoexcitation. Thus, we explore the earliest time processes involved in the interconversion from bound excited state motion over the *B* state onto some dissociative surface leading to the separation of atomic fragments. Within 2 ps in a dense liquid environment, these hot atoms can collide with neighboring solvent molecules, give up some of their energy and perhaps reform an excited iodine molecule in some bound state. We thus concern ourselves specifically with the microscopic description of the solvent interactions and dynamics responsible for both the predissociation and recombination processes central to this early time photoexcited dynamics. In this paper, we will explore these processes in liquid xenon, as a function of solvent density. We believe the qualitative picture we find in this solvent is generally applicable to other nonpolar solvents.

Remarkably, even the earliest time nonadiabatic transitions coupling the bound *B* state motion onto the dissociative surfaces are strongly influenced by the solvent. The excited *B* state motion of free I_2 molecules in the gas phase has been studied in detail[2–5] and the life time of this state under these conditions is on the microsecond time scale.[6] In solution, however, recent ultrafast spectroscopic experiments[7,8] reveal that the *B* state undergoes nonadiabatic predissociation within 200–300 femtoseconds of photoexcitation. This *B* state predissociation thus occurs due to solvent-induced couplings to dissociative states which, in the gas phase, are very weak.

The geminate recombination dynamics after *B* state predissociation is fundamentally nonadiabatic and results from the strong influences of solvent on the couplings between surfaces. Picosecond experiments of Harris and co-workers[9–11] have revealed that recombination occurs in less than 2 ps in a dense liquid environment, and work from various groups[1,9,10,12–15] points to the A' state as being the most likely state into which recombination takes place under these conditions, though *X* and *A* state recombination possibilities have also been considered.[12–14] Recent femtosecond experiments[16,17] on I_2 in rare gas clusters and matrices indicates that solvent caging and recombination in fact occurs very quickly in only about 600 fs and exhibits coherent vibrations on the *A* or A' states. The influence of pressure on I_2 predissociation, geminate recombination, and vibrational relaxation in the gas-to-liquid transition region in a variety of rare gas solvents has recently been explored experimentally.[15,18,19] This last reference also reviews much of the more recent experimental work on this system using femtosecond time resolved techniques. The longer time vibrational relaxation of the recombined I_2 molecule in dense liquid environments has been studied extensively both experimentally[1,11,20,21] and theoretically[22–32] and in this paper we will not consider these longer time processes.

Many early calculations on the geminate recombination and curve crossing dynamics of I_2 in solution used Langevin

dynamics[33–39] methods to treat the effects of a continuum solvent on the excited state motion. These early exploratory studies gave a qualitative understanding of the effects of including dynamics over many coupled surfaces on recombination. The microscopic treatment offered by molecular dynamics methods in principle should provide a complete understanding of the predissociation and geminate recombination process.

Early molecular dynamics (MD) calculations on this system[25,29,31,32,40] were restricted to studies of vibrational relaxation or adiabatic caging dynamics since methods for incorporating electronic transitions in molecular dynamics were not well developed. Recently, however, there have, and continue to be significant developments in this area.[41–77] This paper describes the application of these methods,[43,45,68–70] together with the diatomics in molecules (DIM) semiempirical electronic structure method for describing the many coupled electronic surfaces, to study iodine photodissociation and geminate recombination in solution.

Recent studies have begun to explore the usefulness of DIM like semiempirical electronic structure methods to treat nonadiabatic photodissociation dynamics in condensed phase systems: Gersonde and Gabriel have studied Cl_2 in xenon,[78] and recent studies of p-state atoms in rare-gas matrices by Gerber *et al.*[79,80] are examples. These studies have ignored spin-orbit interactions and used methods which only approximately handle electronic phase coherence during the nonadiabatic dynamics of the system. Apkarian *et al.*[81] have investigated spectroscopy of spin-orbit transitions of iodine atoms in crystalline Xe and Kr as well as the adiabatic dynamics of I_2 in solid Kr following its dissociative excitation on the $A(^2\Pi_{1u})$ surface.[82–87]

The aim of our study is not only to develop an understanding of how solvent influences electronic nonadiabaticity, but also to explore the capabilities of nonadiabatic MD methods and semiempirical electronic structure techniques as applied to studying the dynamics of realistic condensed phase reactions through direct comparisons with experimental findings for this well studied system.

The paper is organized as follows: Our implementation of DIM semiempirical electronic structure techniques to compute the coupled potential energy surfaces of I_2 in solution including the effects of spin-orbit coupling is detailed in ssction II A, use of the DIM eigenvectors and eigenvalues to compute nonadiabatic coupling vectors, nuclear forces for the different electronic potential surfaces, and the electronic subsystem quantal propagator is described in Section II B. In Section II C we summarize our application of the nonadiabatic MD method for this system. The results of our calculations are presented in Section III. First in Section III A, we survey the different channels which our nonadiabatic MD calculations predict are responsible for B state predissociation in solution. Next, in Section III B, we study the properties of the DIM Hamiltonian of the I_2-Xe cluster system to explore whether the predissociation channels predicted from our nonadiabatic MD calculations in solution can be understood in terms of the off-diagonal elements of the bimolecular cluster. Finally, in Section III C we study the longer time dynamics during which the predissociating fragments collide with neighboring solvent molecules and undergo recombination. We study the density dependence of these processes. The paper is concluded in Section IV where we compare the predictions of our calculations with results of ultrafast femtosecond and Raman scattering experiments.

II. METHODS

A. DIM method

The diatomics-in-molecules method (DIM) is a semiempirical approach developed by Ellison[88–90] for computing potential energy surfaces (PES) of the ground and excited states of polyatomic systems from diatomic potentials. It is closely related to the semiempirical extended valence bond (EVB) methods[58,91–98] and is ideally suitable for studies of the dynamics of a variety of chemical reactions.

In our implementation of the method, the Schrödinger equation is formulated in terms of potentials of the constituent atomic and diatomic fragments for the system of an iodine molecule embedded in liquid xenon, which is represented here as $Xe^{(1)}Xe^{(2)}\cdots Xe^{(n)}I^{(1)}I^{(2)}$. Spin-orbit coupling, electron correlation and hyperfine interactions in the iodine molecule are incorporated by using proper potentials for the corresponding electronic states of the molecule.

The time dependent electronic wave function of the polyatomic system, $\psi(t)$, is expanded in terms of a canonical set of valence bond (VB) adiabatic state wave functions, $\phi_k(t)$,

$$\psi(t)=\sum_k a_k(t)\phi_k(t). \tag{2.1}$$

We shall discuss the evolution of the dynamical coefficients $a_k(t)$ later in this section, here however we show how the DIM approach is used to obtain the VB functions ϕ_k.

Within the DIM formulation these VB wave functions, $\phi_k(t)$, are written in terms of polyatomic basis functions (pbf's), Φ_j,

$$\phi_k(t)=\sum_j \Gamma_{kj}\Phi_j, \tag{2.2}$$

where expansion coefficients, Γ_{kj}, are the DIM eigenvectors. The pbf's are products of atomic and diatomic functions, that are ultimately written as linear combinations of simple products of atomic functions (spaf's), and which are assumed to be eigenfunctions of their respective atomic and diatomic Hamiltonians with eigenvalues equal to experimental energies.

Xenon atoms are restricted to be in the ground state and are represented by a single s function since they have an S symmetry closed shell. Iodine atoms have P-symmetry and are represented with ^2P functions. The polyatomic basis functions, Φ_j, are written as antisymmetrized products of S-symmetrical functions of the xenon atoms and $\zeta^{(j)}$ group functions of the iodine molecule,

$$\Phi_j = \hat{A}\zeta^{(j)} \prod_{i=1}^{n} |s^{(i)}\rangle, \tag{2.3}$$

where the index j indicates the electronic state of I_2. The zero overlap of atomic orbitals approximation (ZOAO), allows us to omit the antisymmetrization operator, $\hat{A}$, rendering the polyatomic wave function as a simple product of atomic and diatomic group functions. The error arising from this approximation is proportional to the square of the overlap integrals and has been shown to be small in DIM calculations of halogen atoms in nobel gases.[99]

We limit our basis set to covalent configurations, neglecting ion pair states for the iodine molecule as well as ionic states that involve the positive charge delocalization in the solvent. This is justified by the fact that ionic states lie ~4 eV above any of the states of interest in the early time dynamics in solution.[1,100] The inclusion of ionic states does not present theoretical obstacles but unnecessarily increases the computational effort in the MD simulation.

In our basis set for the I_2 molecule, we include 23 Hund's case (c) covalent molecular states, $\zeta^{(j)}$. These are presented in Table I distributed in three blocks according to their different dissociation limits. They are classified among different symmetry species not only according to case (c) type classification but also according to case (a), (b) or $\Omega - s$ type. The latter has a well defined meaning only for fairly small internuclear separations, R_{I-I}, while the case (c) classification is applicable for large R_{I-I} values and are important for dissociation product correlations. In the first column of Table I we identify electronic states according to the value of the projection of the total angular momentum in the direction of the bond, $\Omega = |M^{(a)} + M^{(b)}|$, which is the only well defined quantum number when the electric field due to the other atom of the molecule is too weak to disrupt the coupling of orbital and spin atomic angular momenta, $L^{(i)}$ and $\mathbf{S}^{(i)}$. In the second column of the table, we summarize expressions for the diatomic wave functions, $\zeta^{(j)}$. Any of these wave functions may be expressed in the basis set of spaf's,

$$\{|J^{(a)}M^{(a)}\rangle|J^{(b)}M^{(b)}\rangle\}$$
$$J^{(a),(b)} = 3/2, 1/2$$
$$M^{(a),(b)} = -J^{(a),(b)}, -J^{(a),(b)}+1, \ldots, J^{(a),(b)} \tag{2.4}$$

by the compact expression

$$\zeta^{(j)} = \sum_{k=1}^{n_j} C_{j,k}\{|J_k^{(a)}M_k^{(a)}\rangle|J_k^{(b)}M_k^{(b)}\rangle\},$$

where n_j is the number of the different products $\{|J_k^{(a)}M_k^{(a)}\rangle|J_k^{(b)}M_k^{(b)}\rangle\}$ involved in $\zeta^{(j)}$ and the $C_{j,k}$ are numerical coefficients summarized in the table. Atomic states, $|J_k M_k\rangle$, are in the total angular momentum representation (coupled representation), where $\mathbf{J} = \mathbf{L} + \mathbf{S}$ and M_k is the projection of $\mathbf{J}$ in the direction of the bond. States with Ω different from zero are double degenerate. Each degenerate state corresponds to one of the two possible orientations for the projection of the total angular momentum in the direction of the bond. Consequently, the 23 Hund's case (c) covalent molecular states form a basis set of 36 states due to degeneracies.

The energy levels of the system are obtained now in the usual way by forming the Hamiltonian matrix of order 36×36.

The neglect of exchange effects allows us to write the molecular basis functions as simple products of the nonoverlapping atomic wave functions of the two interacting iodine atoms. There is a well known scheme for building up these functions and assigning the g/u character in general (or the $+/-$ character when $\Omega = 0$) that can be found in references.[101–103]

Due to the lack of interatomic (atomic-diatomic) electron permutations in the polyatomic functions [ZOAO version of Eq. (2.3)], the Hamiltonian of the system can be partitioned into interatomic and atomic terms according to[98]

$$\hat{H} = \sum_K \sum_{L>K} H^{(KL)} - n\sum_K H^{(K)}, \tag{2.5}$$

where $H^{(K)}$ is the Hamiltonian operator of atom K and contains all kinetic energy operators and intra-atomic potential energy terms that depend solely on the position of atom K and on the coordinates of those electrons initially assigned to this atom. Similarly, $H^{(KL)}$ is the Hamiltonian operator appropriate for the isolated diatomic fragment KL.

The diatomic fragment Hamiltonian for I_2, $H^{I^{(1)}I^{(2)}}$, is constructed from curves of pair potentials of states listed in Table I, that are fitted to experimental results,[104–110] or theoretical calculations,[101,111,112] and which are presented in Fig. 1. These DIM basis states are taken as a diabatic basis for which electronic states with the same symmetry can cross. We thus assume that intramolecular coupling of states with the same symmetry is small compared to intermolecular coupling introduced by the solvent. This approximation is justified by significant differences in predissociation relaxation rates observed in the gas phase and liquid solutions.[2,7,8]

The Hamiltonian for the diatomic fragments $I^{(i)}Xe^{(j)}$ is constructed from empirical potentials[113] of the usual Σ, Π and $\overline{\Pi}$ orientations as described in reference.[114] The vector Σ is oriented along the $\mathbf{R}_{ij}$ vector, Π is perpendicular to Σ and located in the plane formed by $\mathbf{R}_{ij}$ and the x axis, while $\overline{\Pi}$ is perpendicular to this plane (see Fig. 2).

In the reference frame of the diatomic fragment this Hamiltonian is

$$H^{I^{(i)}Xe^{(j)}} = \begin{bmatrix} V_\Pi & 0 & 0 \\ 0 & V_{\overline{\Pi}} & 0 \\ 0 & 0 & V_\Sigma \end{bmatrix}. \tag{2.6}$$

In order to express this Hamiltonian in the basis set of the coupled representation of Eq. (2.4), we first transform it from the p states defined in the reference frame of the diatomic fragment, $(p_\Pi, p_{\overline{\Pi}}, p_\Sigma)$, to the fixed reference frame of the laboratory, (p_x, p_y, p_z), according to the transformation

$$DH^{I^{(i)}Xe^{(j)}}D^{-1}, \tag{2.7}$$

TABLE I. Molecular orbitals of I_2.

Case c type	Case c type wave function	Case a or b or $\Omega-s$ type
0_g^+	$1/\sqrt{2}\{\lvert\frac{3}{2}\frac{1}{2}\rangle\lvert\frac{3}{2}-\frac{1}{2}\rangle-\lvert\frac{3}{2}-\frac{1}{2}\rangle\lvert\frac{3}{2}\frac{1}{2}\rangle\}$	$X,1^1\Sigma_g^+$
0_g^+	$1/\sqrt{2}\{\lvert\frac{3}{2}\frac{3}{2}\rangle\lvert\frac{3}{2}-\frac{3}{2}\rangle-\lvert\frac{3}{2}-\frac{3}{2}\rangle\lvert\frac{3}{2}\frac{3}{2}\rangle\}$	$a',^3\Sigma_g^-$
0_u^-	$1/\sqrt{2}\{\lvert\frac{3}{2}\frac{3}{2}\rangle\lvert\frac{3}{2}-\frac{3}{2}\rangle+\lvert\frac{3}{2}-\frac{3}{2}\rangle\lvert\frac{3}{2}\frac{3}{2}\rangle\}$	$^3\Pi_u$
0_u^-	$1/\sqrt{2}\{\lvert\frac{3}{2}\frac{1}{2}\rangle\lvert\frac{3}{2}-\frac{1}{2}\rangle+\lvert\frac{3}{2}-\frac{1}{2}\rangle\lvert\frac{3}{2}\frac{1}{2}\rangle\}$	$1^3\Sigma_u^+$
1_g	$1/\sqrt{2}\{\lvert\frac{3}{2}\frac{3}{2}\rangle\lvert\frac{3}{2}-\frac{1}{2}\rangle-\lvert\frac{3}{2}-\frac{1}{2}\rangle\lvert\frac{3}{2}\frac{3}{2}\rangle\}$	$a,^3\Pi_g$
	$1/\sqrt{2}\{\lvert\frac{3}{2}-\frac{3}{2}\rangle\lvert\frac{3}{2}\frac{1}{2}\rangle-\lvert\frac{3}{2}\frac{1}{2}\rangle\lvert\frac{3}{2}-\frac{3}{2}\rangle\}$	
1_u	$1/\sqrt{2}\{\lvert\frac{3}{2}\frac{3}{2}\rangle\lvert\frac{3}{2}-\frac{1}{2}\rangle+\lvert\frac{3}{2}-\frac{1}{2}\rangle\lvert\frac{3}{2}\frac{3}{2}\rangle\}$	$A,^3\Pi_{1u}^+$
	$1/\sqrt{2}\{\lvert\frac{3}{2}-\frac{3}{2}\rangle\lvert\frac{3}{2}\frac{1}{2}\rangle+\lvert\frac{3}{2}\frac{1}{2}\rangle\lvert\frac{3}{2}-\frac{3}{2}\rangle\}$	
1_u	$\{\lvert\frac{3}{2}\frac{1}{2}\rangle\lvert\frac{3}{2}\frac{1}{2}\rangle\}$	$^1\Pi_u$
	$\{\lvert\frac{3}{2}-\frac{1}{2}\rangle\lvert\frac{3}{2}-\frac{1}{2}\rangle\}$	
2_g	$1/\sqrt{2}\{\lvert\frac{3}{2}\frac{3}{2}\rangle\lvert\frac{3}{2}\frac{1}{2}\rangle-\lvert\frac{3}{2}\frac{1}{2}\rangle\lvert\frac{3}{2}\frac{3}{2}\rangle\}$	$^3\Pi_g$
	$1/\sqrt{2}\{\lvert\frac{3}{2}-\frac{3}{2}\rangle\lvert\frac{3}{2}-\frac{1}{2}\rangle-\lvert\frac{3}{2}-\frac{1}{2}\rangle\lvert\frac{3}{2}-\frac{3}{2}\rangle\}$	
2_u	$1/\sqrt{2}\{\lvert\frac{3}{2}\frac{3}{2}\rangle\lvert\frac{3}{2}\frac{1}{2}\rangle+\lvert\frac{3}{2}\frac{1}{2}\rangle\lvert\frac{3}{2}\frac{3}{2}\rangle\}$	$A',^3\Pi_u$
	$1/\sqrt{2}\{\lvert\frac{3}{2}-\frac{3}{2}\rangle\lvert\frac{3}{2}-\frac{1}{2}\rangle+\lvert\frac{3}{2}-\frac{1}{2}\rangle\lvert\frac{3}{2}-\frac{3}{2}\rangle\}$	
3_u	$\{\lvert\frac{3}{2}\frac{3}{2}\rangle\lvert\frac{3}{2}\frac{3}{2}\rangle\}$	$^3\Delta_u$
	$\{\lvert\frac{3}{2}-\frac{3}{2}\rangle\lvert\frac{3}{2}-\frac{3}{2}\rangle\}$	
0_g^+	$\frac{1}{2}\{\lvert\frac{3}{2}\frac{1}{2}\rangle\lvert\frac{1}{2}-\frac{1}{2}\rangle-\lvert\frac{1}{2}-\frac{1}{2}\rangle\lvert\frac{3}{2}\frac{1}{2}\rangle+\lvert\frac{3}{2}-\frac{1}{2}\rangle\lvert\frac{1}{2}\frac{1}{2}\rangle-\lvert\frac{1}{2}\frac{1}{2}\rangle\lvert\frac{3}{2}-\frac{1}{2}\rangle\}$	$^3\Pi_g$
0_g^-	$\frac{1}{2}\{\lvert\frac{3}{2}\frac{1}{2}\rangle\lvert\frac{1}{2}-\frac{1}{2}\rangle-\lvert\frac{1}{2}-\frac{1}{2}\rangle\lvert\frac{3}{2}\frac{1}{2}\rangle-\lvert\frac{3}{2}-\frac{1}{2}\rangle\lvert\frac{1}{2}\frac{1}{2}\rangle+\lvert\frac{1}{2}\frac{1}{2}\rangle\lvert\frac{3}{2}-\frac{1}{2}\rangle\}$	$^3\Pi_g$
0_u^+	$\frac{1}{2}\{\lvert\frac{3}{2}\frac{1}{2}\rangle\lvert\frac{1}{2}-\frac{1}{2}\rangle+\lvert\frac{1}{2}-\frac{1}{2}\rangle\lvert\frac{3}{2}\frac{1}{2}\rangle+\lvert\frac{3}{2}-\frac{1}{2}\rangle\lvert\frac{1}{2}\frac{1}{2}\rangle+\lvert\frac{1}{2}\frac{1}{2}\rangle\lvert\frac{3}{2}-\frac{1}{2}\rangle\}$	$B,^3\Pi_u$
0_u^-	$\frac{1}{2}\{\lvert\frac{3}{2}\frac{1}{2}\rangle\lvert\frac{1}{2}-\frac{1}{2}\rangle+\lvert\frac{1}{2}-\frac{1}{2}\rangle\lvert\frac{3}{2}\frac{1}{2}\rangle-\lvert\frac{3}{2}-\frac{1}{2}\rangle\lvert\frac{1}{2}\frac{1}{2}\rangle-\lvert\frac{1}{2}\frac{1}{2}\rangle\lvert\frac{3}{2}-\frac{1}{2}\rangle\}$	$^1\Sigma_u^-$
1_g	$1/\sqrt{2}\{\lvert\frac{3}{2}\frac{3}{2}\rangle\lvert\frac{1}{2}-\frac{1}{2}\rangle-\lvert\frac{1}{2}-\frac{1}{2}\rangle\lvert\frac{3}{2}\frac{3}{2}\rangle\}$	$^1\Pi_g$
	$1/\sqrt{2}\{\lvert\frac{3}{2}-\frac{3}{2}\rangle\lvert\frac{1}{2}\frac{1}{2}\rangle-\lvert\frac{1}{2}\frac{1}{2}\rangle\lvert\frac{3}{2}-\frac{3}{2}\rangle\}$	
1_g	$1/\sqrt{2}\{\lvert\frac{3}{2}\frac{1}{2}\rangle\lvert\frac{1}{2}\frac{1}{2}\rangle-\lvert\frac{1}{2}\frac{1}{2}\rangle\lvert\frac{3}{2}\frac{1}{2}\rangle\}$	$^3\Sigma_g^-$
	$1/\sqrt{2}\{\lvert\frac{3}{2}-\frac{1}{2}\rangle\lvert\frac{1}{2}-\frac{1}{2}\rangle-\lvert\frac{1}{2}-\frac{1}{2}\rangle\lvert\frac{3}{2}-\frac{1}{2}\rangle\}$	
1_u	$1/\sqrt{2}\{\lvert\frac{3}{2}\frac{3}{2}\rangle\lvert\frac{1}{2}-\frac{1}{2}\rangle+\lvert\frac{1}{2}-\frac{1}{2}\rangle\lvert\frac{3}{2}\frac{3}{2}\rangle\}$	$1^3\Sigma_u^+$
	$1/\sqrt{2}\{\lvert\frac{3}{2}-\frac{3}{2}\rangle\lvert\frac{1}{2}\frac{1}{2}\rangle+\lvert\frac{1}{2}\frac{1}{2}\rangle\lvert\frac{3}{2}-\frac{3}{2}\rangle\}$	
1_u	$1/\sqrt{2}\{\lvert\frac{3}{2}\frac{1}{2}\rangle\lvert\frac{1}{2}\frac{1}{2}\rangle+\lvert\frac{1}{2}\frac{1}{2}\rangle\lvert\frac{3}{2}\frac{1}{2}\rangle\}$	$2^3\Sigma_u^+$
	$1/\sqrt{2}\{\lvert\frac{3}{2}-\frac{1}{2}\rangle\lvert\frac{1}{2}-\frac{1}{2}\rangle+\lvert\frac{1}{2}-\frac{1}{2}\rangle\lvert\frac{3}{2}-\frac{1}{2}\rangle\}$	
2_g	$1/\sqrt{2}\{\lvert\frac{3}{2}\frac{3}{2}\rangle\lvert\frac{1}{2}\frac{1}{2}\rangle-\lvert\frac{1}{2}\frac{1}{2}\rangle\lvert\frac{3}{2}\frac{3}{2}\rangle\}$	$^1\Delta_g$
	$1/\sqrt{2}\{\lvert\frac{3}{2}-\frac{3}{2}\rangle\lvert\frac{1}{2}-\frac{1}{2}\rangle-\lvert\frac{1}{2}-\frac{1}{2}\rangle\lvert\frac{3}{2}-\frac{3}{2}\rangle\}$	
2_u	$1/\sqrt{2}\{\lvert\frac{3}{2}\frac{3}{2}\rangle\lvert\frac{1}{2}\frac{1}{2}\rangle+\lvert\frac{1}{2}\frac{1}{2}\rangle\lvert\frac{3}{2}\frac{3}{2}\rangle\}$	$^3\Delta_u$
	$1/\sqrt{2}\{\lvert\frac{3}{2}-\frac{3}{2}\rangle\lvert\frac{1}{2}-\frac{1}{2}\rangle+\lvert\frac{1}{2}-\frac{1}{2}\rangle\lvert\frac{3}{2}-\frac{3}{2}\rangle\}$	
0_g^+	$1/\sqrt{2}\{\lvert\frac{1}{2}\frac{1}{2}\rangle\lvert\frac{1}{2}-\frac{1}{2}\rangle-\lvert\frac{1}{2}-\frac{1}{2}\rangle\lvert\frac{1}{2}\frac{1}{2}\rangle\}$	$2^1\Sigma_g^-$
0_u^-	$1/\sqrt{2}\{\lvert\frac{1}{2}\frac{1}{2}\rangle\lvert\frac{1}{2}-\frac{1}{2}\rangle+\lvert\frac{1}{2}-\frac{1}{2}\rangle\lvert\frac{1}{2}\frac{1}{2}\rangle\}$	$2^3\Sigma_u^+$
1_u	$\{\lvert\frac{1}{2}\frac{1}{2}\rangle\lvert\frac{1}{2}\frac{1}{2}\rangle\}$	$^3\Delta_u$
	$\{\lvert\frac{1}{2}-\frac{1}{2}\rangle\lvert\frac{1}{2}-\frac{1}{2}\rangle\}$	

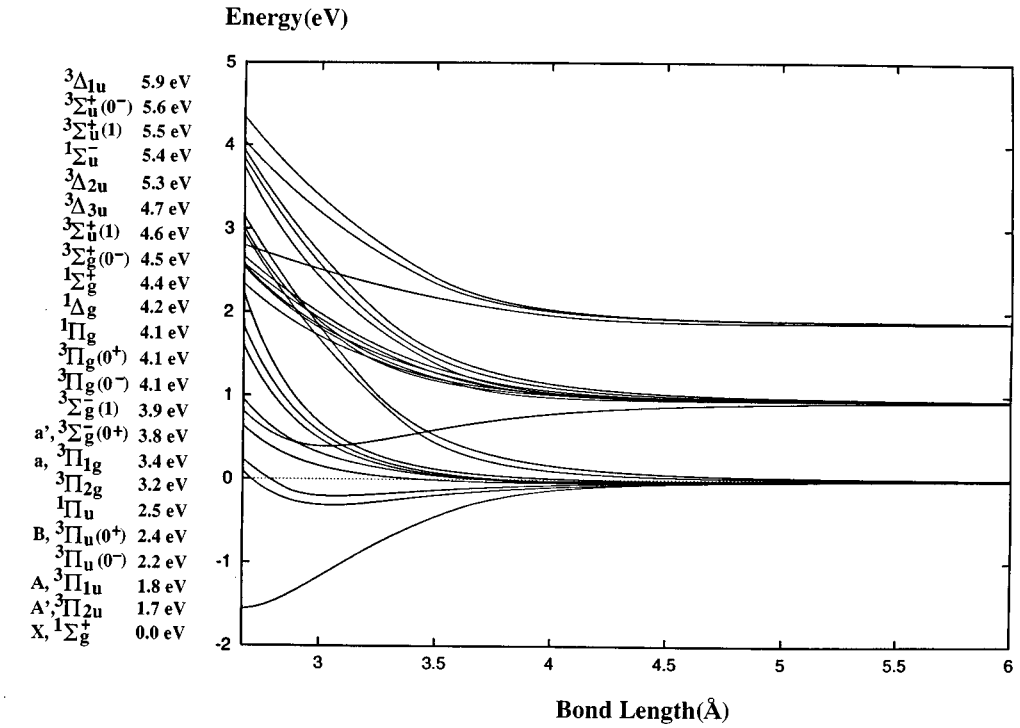

FIG. 1. Gas phase I_2 potential energy surfaces obtained from various experiments and calculations as described in the text.

where D is the Cartesian rotation matrix with row vectors constructed from the projections of the unit vectors $\hat{x}$, $\hat{y}$, and $\hat{z}$ along the Π, $\overline{\Pi}$, and Σ axes (see Fig. 2):

$$D=\begin{bmatrix} \sin(\alpha) & 0 & \cos(\alpha) \\ -\cos(\beta)\cos(\alpha) & \sin(\beta) & \cos(\beta)\sin(\alpha) \\ -\sin(\beta)\cos(\alpha) & -\cos(\beta) & \sin(\beta)\sin(\alpha) \end{bmatrix}. \quad (2.8)$$

The Hamiltonian $H^{I^{(i)}Xe^{(j)}}$ expressed in the basis set of p states defined in the fixed reference frame of the laboratory, (p_x, p_y, p_z), is then transformed to the p basis functions defined in the reference frame of the iodine molecule according to the transformation defined by Eq. (2.7) where the new transformation matrix, D, is defined as the inverse of the Cartesian rotation matrix presented above, where now i and j correspond to atoms $I^{(1)}$ and $I^{(2)}$.

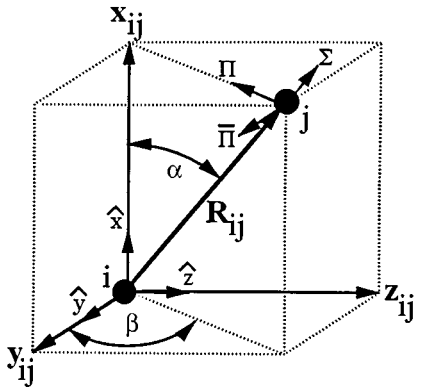

FIG. 2. Coordinate systems defining rotation matrices which transform p-orbital basis functions in molecular frame to laboratory frame.

This Hamiltonian, $H^{I^{(i)}Xe^{(j)}}$, is then transformed to the complex p basis functions, (p_1, p_0, p_{-1}), defined by

$$\begin{aligned} p_1&=[p_x+ip_y]/\sqrt{2}, \\ p_0&=p_z, \\ p_{-1}&=[p_x-ip_y]/\sqrt{2} \end{aligned} \quad (2.9)$$

according to the transformation defined by Eq. (2.7) where this next transformation matrix, D, is defined as follows:

$$D=\begin{bmatrix} 1/\sqrt{2} & i/\sqrt{2} & 0 \\ 0 & 0 & 1 \\ 1/\sqrt{2} & -i/\sqrt{2} & 0 \end{bmatrix}. \quad (2.10)$$

$H^{I^{(i)}Xe^{(j)}}$ is now a 3×3 matrix in the complex $|m_l\rangle$ basis set. In order to express it in the 6×6 uncoupled representation, $|m_l\ m_s\rangle$, we must perform the outer product with the 2×2 identity matrix, $\hat{\mathbf{1}}_2$, according to

$$H\otimes\hat{\mathbf{1}}_2=\begin{bmatrix} H_{11} & 0 & H_{12} & 0 & H_{13} & 0 \\ 0 & H_{11} & 0 & H_{12} & 0 & H_{13} \\ H_{21} & 0 & H_{22} & 0 & H_{23} & 0 \\ 0 & H_{21} & 0 & H_{22} & 0 & H_{23} \\ H_{31} & 0 & H_{32} & 0 & H_{33} & 0 \\ 0 & H_{31} & 0 & H_{32} & 0 & H_{33} \end{bmatrix}. \quad (2.11)$$

Finally the Hamiltonian is expressed in the coupled representation, $|JM\rangle$, according to the transformation defined by Eq. (2.7), where D is the Clebsh–Gordon matrix defined in the transformation expression below

$$|J\ \ M\rangle \quad = \quad D \quad |m_l\ \ m_s\rangle$$

$$\begin{bmatrix} |3/2 & 3/2\rangle \\ |3/2 & 1/2\rangle \\ |3/2 & -1/2\rangle \\ |3/2 & -3/2\rangle \\ |1/2 & 1/2\rangle \\ |1/2 & -1/2\rangle \end{bmatrix} = \begin{bmatrix} 1 & 0 & 0 & 0 & 0 & 0 \\ 0 & \sqrt{1/3} & \sqrt{2/3} & 0 & 0 & 0 \\ 0 & 0 & 0 & \sqrt{2/3} & \sqrt{1/3} & 0 \\ 0 & 0 & 0 & 0 & 0 & 1 \\ 0 & \sqrt{2/3} & -\sqrt{1/3} & 0 & 0 & 0 \\ 0 & 0 & 0 & \sqrt{1/3} & -\sqrt{2/3} & 0 \end{bmatrix} \begin{bmatrix} |1 & 1/2\rangle \\ |1 & -1/2\rangle \\ |0 & 1/2\rangle \\ |0 & -1/2\rangle \\ |-1 & 1/2\rangle \\ |-1 & -1/2\rangle \end{bmatrix}. \tag{2.12}$$

Rare gas atoms interact according to their s-ground state charge distributions. We represent these interactions with a Lennard-Jones potential with $\epsilon = 220$ K and $\sigma = 3.977$ Å.

The total Hamiltonian is written as the direct sum over all diatomic-fragment Hamiltonians of the system:

$$H = H^{(I^{(1)}I^{(2)})} + \hat{\mathbf{1}}_6 \otimes \sum_{k=1}^{n} H^{\mathrm{I}^{(1)}\mathrm{Xe}^{(k)}} + \sum_{k=1}^{n} H^{\mathrm{I}^{(2)}Xe^{(k)}} \otimes \hat{\mathbf{1}}_6 + \hat{\mathbf{1}}_{36} \otimes \sum_{i=1}^{n-1} \sum_{j>i}^{n} V^{\mathrm{Xe}^{(i)}\mathrm{Xe}^{(j)}}, \tag{2.13}$$

where the constant monoatomic contribution appearing in Eq. (2.5) is omitted. The energy of the system is calculated relative to the energy of infinitely separated atoms in the ground state:

$$E_\infty = 2E_{I[^2P_{3/2}]} + \sum_{j=1}^{n} E_{\mathrm{Xe}}. \tag{2.14}$$

For a minimum effort, the polyatomic energies are calculated by a simple diagonalization procedure requiring no electronic integral evaluations.

This method neglects three and four center terms in the Hamiltonian matrix as well as the nonorthogonality of the basis set and the overlap between atomic orbitals belonging to different rare gas atoms or solvent-iodine molecule overlap. These approximations are very common in semiempirical methods, in particular in the DIM method.[99]

In Fig. 3, we show PES of our implementation of the DIM model for I_2 in a perfect xenon fcc crystal. Iodine atoms are placed on the [1,0,0] axis at a distance $R_{\mathrm{I-I}}$ from each other, keeping the center of mass fixed at the substitutional site. Fig. 4 shows analogous results for the [1,1,0] axis. From these figures we see evidence of coupling between states as they repel one another. The Frank–Condon region in this crystal, at $\rho^* = 0.7$, is largely unchanged from the gas phase results of Fig. 1. Finally, at large $R_{\mathrm{I-I}}$ we see high energy configurations associated with I−Xe collisions.

Independent work by Buchachenko *et al.* using a closely related formulation of the DIM method to study the $I_2 - Ar$ cluster system has recently been reported.[115] Results seem qualitatively similar to our findings on the cluster system reported in Section III B.

B. Computation of approximate nonadiabatic coupling vectors, adiabatic forces, and the adiabatic basis set propagator with DIM

As will be outlined in section II C to implement the surface hopping algorithm, we need to compute the nonadiabatic coupling vectors which can be written in terms of the adiabatic VB states as follows:

$$\mathbf{D}_{mn} = \langle \phi_m | \nabla_{\mathbf{R}} | \phi_n \rangle = - \frac{\langle \phi_m | \nabla_{\mathbf{R}} H | \phi_n \rangle}{(\epsilon_m - \epsilon_n)} \quad \forall n \neq m. \tag{2.15}$$

This is easily shown as discussed in reference 69. Expanding the VB states in terms of the pbf's according to Eq. (2.2) we find the following expression for the nonadiabatic coupling vector

$$\mathbf{D}_{mn} = - \frac{\Sigma_i \Sigma_j \Gamma^*_{mi} \Gamma_{nj} \langle \Phi_i | \nabla_{\mathbf{R}} H | \Phi_j \rangle}{(\epsilon_m - \epsilon_n)}. \tag{2.16}$$

We can simplify the above result by making use of the following identity:

$$\nabla_{\mathbf{R}} \langle \Phi_i | H | \Phi_j \rangle = \langle \nabla_{\mathbf{R}} \Phi_i | H | \Phi_j \rangle + \langle \Phi_i | H | \nabla_{\mathbf{R}} \Phi_j \rangle + \langle \Phi_i | \nabla_{\mathbf{R}} H | \Phi_j \rangle. \tag{2.17}$$

The left hand side of this equation is easily evaluated since we have given explicit (though somewhat complicated) expressions for the matrix elements of the Hamiltonian in the pbf basis in Section II A. Evaluation of the terms on the right-hand side of the above result requires explicit knowledge of the pbf's which we don't have as DIM only requires specification of Hamiltonian matrix elements. However, in low energy collision processes, nonadiabatic transitions are associated with distinct changes of electronic character. Since the pbf's are intended to reflect only gradual distor-

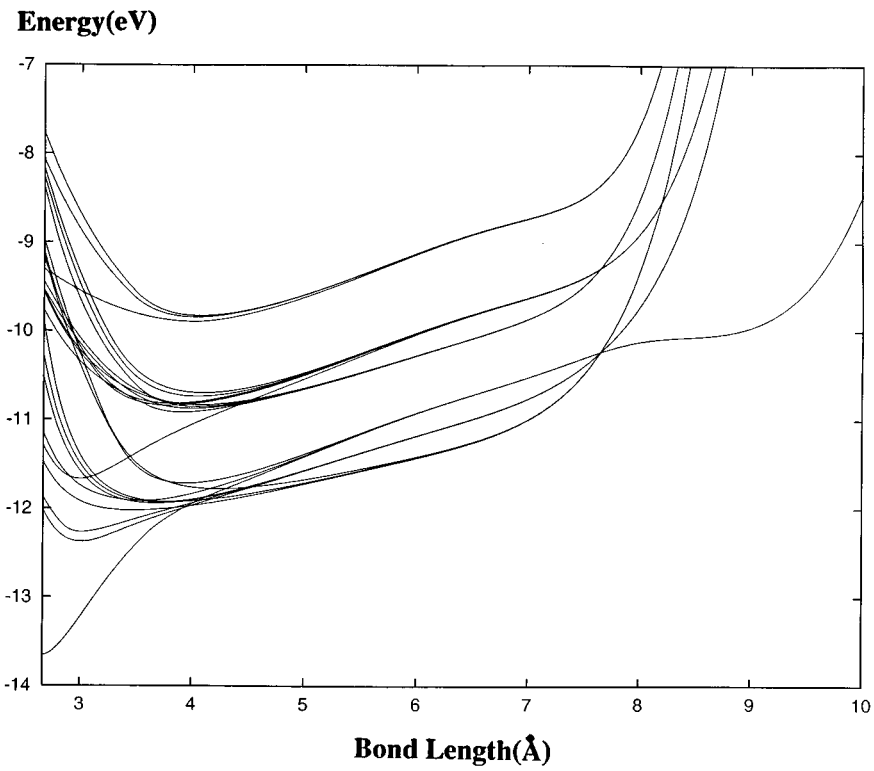

FIG. 3. Potential surfaces as functions of R_{I-I} computed with DIM Hamiltonian for I_2 center-of-mass positioned on a lattice site of an FCC crystal of xenon with density $\rho^* = 0.7$. I_2 bond is extended along the (100) direction in the crystal.

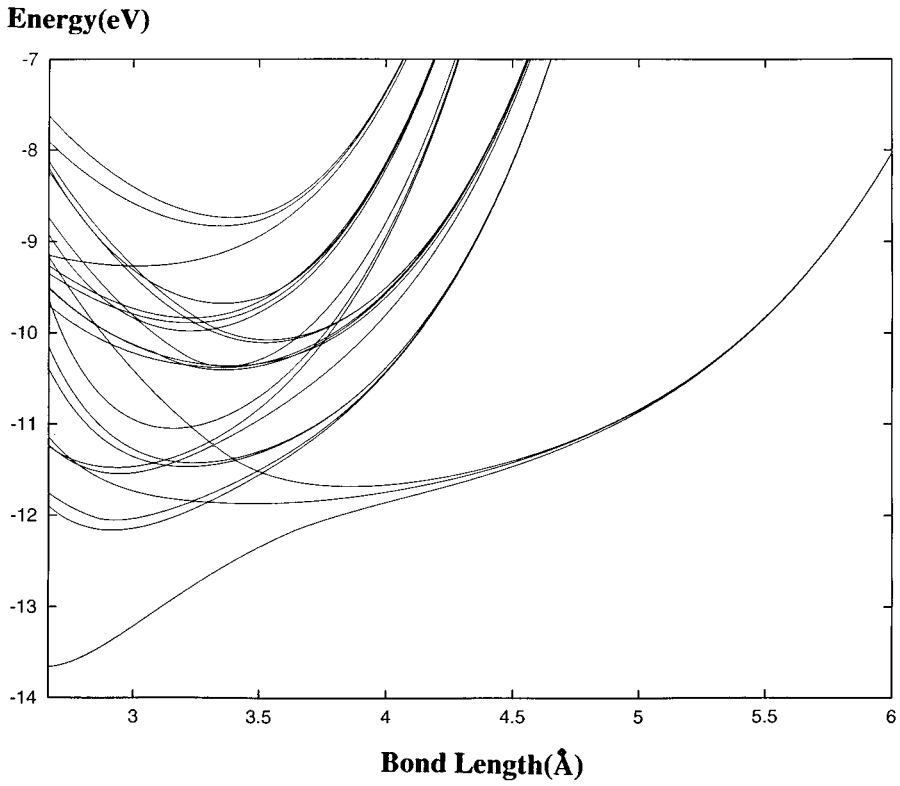

FIG. 4. Same as Fig. 3 except bond is extended along (110) direction of crystal.

tions, we can neglect the first two terms on the right hand side of Eq. (2.17). This amounts to assuming that the polyatomic basis functions change slowly with nuclear coordinates compared to the rate at which the Hamiltonian changes with nuclear motion. These same ideas have proved very valuable for describing several low-energy molecular collision processes.[98] With this assumption we readily arrive at the following approximation for the nonadiabatic coupling vector, now expressed in terms of the DIM eigenvectors, eigenvalues and gradients of the Hamiltonian matrix elements in the pbf basis:

$$\mathbf{D}_{mn} \approx -\frac{\Sigma_i \Sigma_j \Gamma^*_{mi} \Gamma_{nj} \nabla_{\mathbf{R}} \langle \Phi_i | H | \Phi_j \rangle}{(\epsilon_m - \epsilon_n)}. \tag{2.18}$$

The forces which we use to determine the dynamics of the classical particles arise from the charge distribution of the instantaneously occupied state valence bond wave function ϕ_k and the force vector in this state is just the negative of $\nabla_{\mathbf{R}} \epsilon_k = \nabla_{\mathbf{R}} \langle \phi_k | H | \phi_k \rangle = \langle \phi_k | \nabla_{\mathbf{R}} H | \phi_k \rangle$, where the ϵ_k are the eigenvalues of the set of orthonormal functions $\{\phi_k\}$. Substituting Eq. (2.2) we find that the forces are determined by

$$\nabla_{\mathbf{R}} \epsilon_k = \sum_i \sum_j \Gamma^*_{ki} \Gamma_{kj} \langle \Phi_i | \nabla_{\mathbf{R}} H | \Phi_j \rangle. \tag{2.19}$$

Applying the same arguments concerning the slow variation of the pbf's which we used to simplify our expressions for the nonadiabatic coupling vector, the forces can be approximated as

$$\nabla_{\mathbf{R}} \epsilon_k \approx \sum_i \sum_j \Gamma^*_{ki} \Gamma_{kj} \nabla_{\mathbf{R}} \langle \Phi_i | H | \Phi_j \rangle. \tag{2.20}$$

As an independent test of the approximations underlying the above result (the slow variation of the pbf's with nuclear coordinates), we have computed the forces by finite difference estimation and find that the force obtained from Eq. (2.20) is very accurate for typical fluid configurations.

The gradients of the DIM Hamiltonian matrix elements in the pbf basis set in Eq. (2.20) or Eq. (2.18) are most conveniently computed using finite difference though they can be computed exactly as indicated above by differentiating the necessary transformation matrices and the empirical potential energy matrices. For every interacting pair a new set of matrices and the necessary derivatives need to be computed and multiplied. We find that a three point finite difference approach is accurate and comparable in computational expense, and much easier to code for general applications.

The final quantity we need to implement the surface hopping algorithm which will be outlined in section II C is the electronic subsystem propagator. We find it convenient to work with instantaneous adiabatic VB basis states whose coefficient vector $\mathbf{a}(t)$ given in Eq. (2.1) is readily propagated over the short interval t to $t+\delta$ using

$$\mathbf{a}(t+\delta) = \mathbf{T}(t+\delta, t)\mathbf{a}(t), \tag{2.21}$$

where the propagator matrix elements are easily constructed from the instantaneous eigenvalues $\epsilon_n(t)$ and VB eigenfunctions $\phi_n(t)$ using the following short-time approximation:

$$\mathbf{T}_{no}(t+\delta, t) = \exp\left[\frac{-i\delta}{2\hbar}(\epsilon_n(t+\delta) + \epsilon_o(t))\right] \times \langle \phi_n(t+\delta) | \phi_o(t) \rangle. \tag{2.22}$$

Using the pbf expansion of the adiabatic VB states in Eq. (2.2), the overlap matrix element in Eq. (2.22) for the propagator is

$$\langle \phi_n(t+\delta) | \phi_o(t) \rangle = \sum_i \sum_j \Gamma^*_{ni}(t+\delta) \Gamma_{oj}(t) \times \langle \Phi_i(t+\delta) | \Phi_j(t) \rangle. \tag{2.23}$$

To simplify this expression we again make use of the assumption that the pbf's are slowly varying so they do not change much during δ. This assumption, together with the ZOAO approximation enable us to approximately write $\langle \Phi_i(t+\delta) | \Phi_j(t) \rangle \approx \delta_{ij}$. Thus, we employ the approximate result

$$\langle \phi_n(t+\delta) | \phi_o(t) \rangle \approx \sum_i \Gamma^*_{ni}(t+\delta) \Gamma_{oi}(t) \tag{2.24}$$

together with the DIM eigenvalues to compute an approximation to the short time propagator given in Eq. (2.22) as

$$\mathbf{T}_{no}(t+\delta, t) \approx \exp\left[\frac{-i\delta}{2\hbar}(\epsilon_n(t+\delta) + \epsilon_o(t))\right] \times \sum_i \Gamma^*_{ni}(t+\delta) \Gamma_{oi}(t). \tag{2.25}$$

C. The nonadiabatic MD method

The surface hopping algorithm we use here has been presented in detail elsewhere[69,70] and our implementation of this approach incorporating the DIM semiempirical method of electronic structure calculation described in Section II A and the approximate results given in Section II B can be summarized as follows:

We assume that the DIM Hamiltonian in the pbf basis varies linearly with time over a nuclear timestep Δ. In our application this assumption serves simply as a computational convenience to reduce the frequency with which we compute the DIM Hamiltonian. As mentioned earlier, establishing and performing the rotation and transformation matrix multiplies for all the necessary interacting pairs as described in Section II A can be time consuming. As a first guess we assume that the DIM Hamiltonian can be linearly extrapolated over the interval $t \to t+\Delta$ using information from the previous time step, so we approximate the DIM Hamiltonian at some time $t + l\delta$ in new interval as

$$H_{ij}(t + l\delta) = H_{ij}(t) + \Delta H_{ij} \frac{l\delta}{\Delta} \tag{2.26}$$

with

$$\Delta H_{ij}=H_{ij}(t)-H_{ij}(t-\Delta), \tag{2.27}$$

and we have divided the classical timestep Δ up into N_q quantal steps $\delta=\Delta/N_q$. We use this short time step to accurately evolve the quantal subsystem mixed state wave function $\psi(t)$ which can change rapidly on the classical nuclear timescale. We diagonalize the approximate DIM Hamiltonian at all the intermediate points between t and $t+\Delta$ and compute the short time propagators over this interval using these results in Eq. (2.25). Care must be taken to keep track of the phase of the DIM eigenvectors obtained by numerical diagonalization when they are used to compute the propagator. We fix the arbitrary eigenvector phase at its initial value throughout our calculations using the approach described by Xiao and Coker.[116]

Next, we evolve the expansion coefficients $\{a_k(t)\}$ of the mixed state wave function $\psi(t)$ through the sequence of small steps from t to $t+\Delta$. At each quantum time step δ, we use the time dependent expansion coefficients and the propagator matrix elements to compute Tully's fewest switches Monte Carlo transition probabilities. Thus, if state i is occupied and the components of the flux of probability out of state i and into other states k are negative, i.e.,

$$[a_i^*(t+\delta)T_{ik}^f(t+\delta,t)a_k(t)-a_i^*(t-\delta)T_{ik}^b(t-\delta,t)a_k(t)]<0. \tag{2.28}$$

We make transitions out of state i into the various unoccupied states k with probability

$$g_{ki}=-\left[\frac{a_i^*(t+\delta)T_{ik}^f(t+\delta,t)a_k(t)-a_i^*(t-\delta)T_{ik}^b(t-\delta,t)a_k(t)}{a_i^*(t)a_i(t)}\right], \tag{2.29}$$

where the elements of the forward and backward propagators are computed using the approximate result in Eq. (2.25). This result is easily derived using the finite difference approximation

$$\dot{\rho}_{ii}(t)=\frac{\rho_{ii}(t+\delta)-\rho_{ii}(t-\delta)}{2\delta} \tag{2.30}$$

for the time derivative of the diagonal elements of the density matrix $\rho_{ii}(t)=a_i^*(t)a_i(t)$ and proceeding similarly to references.[43,68]

If no trial nonadiabatic Monte Carlo transitions are accepted during all the N_q quantum subsystem steps with in Δ, the quantum system remains in state α and we use the following Verlet equations to advance the classical subsystem:

$$\mathbf{v}_i(t)=\mathbf{v}_i(t-\Delta)+\Delta(\mathbf{F}_{\alpha\alpha}^i(t-\Delta)+\mathbf{F}_{\alpha\alpha}^i(t))/2M_i, \tag{2.31}$$

$$\mathbf{R}_i(t+\Delta)=\mathbf{R}_i(t)+\mathbf{v}_i(t)\Delta+\Delta^2\mathbf{F}_{\alpha\alpha}^i(t)/2M_i. \tag{2.32}$$

Here, $\mathbf{F}_{\alpha\alpha}=-\nabla_{\mathbf{R}}\epsilon_\alpha$ as determined by Eq. (2.20).

If, on the other hand, the various Monte Carlo trials have resulted in a change of state to β during the time interval Δ, the classical system must evolve under the influence of the changing quantum state distribution. Under these circumstances, we use the following approximate transition force:[69,70]

$$\mathbf{F}_{mn}^P(t)\sim-\left\{\frac{(E_m(t)-E_n(t))}{(\hat{\mathbf{D}}_{mn}(t)\cdot\mathbf{v}(t))d}\right\}\hat{\mathbf{D}}_{mn}(t). \tag{2.33}$$

This force is implemented by adjusting the nuclear velocities according to the following result[45,70]

$$\mathbf{v}_i(t)=\mathbf{v}_i(t-\Delta)-\frac{c}{M_i}\hat{\mathbf{D}}_{\beta\alpha}^i(t), \tag{2.34}$$

where we use the value of c with smallest magnitude obtained from the following expression:

$$c_\pm=\frac{\mathbf{v}(t-\Delta)\cdot\hat{\mathbf{D}}_{\beta\alpha}\pm\sqrt{(\mathbf{v}(t-\Delta)\cdot\hat{\mathbf{D}}_{\beta\alpha})^2-2(\mathbf{e}_{\beta\alpha}\cdot\hat{\mathbf{D}}_{\beta\alpha})(E_\beta-E_\alpha)}}{\mathbf{e}_{\beta\alpha}\cdot\hat{\mathbf{D}}_{\beta\alpha}}. \tag{2.35}$$

The dot products in this result involve sums over the components of the entire system vectors. Alternatively, if Eq. (2.35) gives complex solutions we abandon the attempted transition as there is insufficient energy in the classical coordinates coupled to the transition to make up the energy gap and we choose c as follows:[45,70]

$$c=2\mathbf{v}(t-\Delta)\cdot D_{\beta\alpha}/\mathbf{e}_{\beta\alpha}\cdot\hat{\mathbf{D}}_{\beta\alpha}. \tag{2.36}$$

Once new velocities $\mathbf{v}(t)$ are determined, according to the approach outlined above, the positions are advanced using the result

$$\mathbf{R}_i(t+\Delta)=\mathbf{R}_i(t)+\mathbf{v}_i(t)\Delta+\Delta^2\mathbf{F}_{nn}^i(t)/2M_i, \tag{2.37}$$

where $\mathbf{F}_{nn}^i(t)$ is the diagonal element of the force matrix for the newly occupied adiabatic state n.

Finally, we establish the full DIM Hamiltonian at the new configuration $\mathbf{R}(t+\Delta)$ and diagonalize it to obtain new DIM eigenvalues and eigenvectors. In principle, we could re-extrapolate the quantum subsystem dynamics now using

$$\Delta H_{ij} = H_{ij}(t+\Delta) - H_{ij}(t) \tag{2.38}$$

in Eq. (2.26) to reintegrate and correct the expansion coefficient propagation giving accurate coherent integration of the mixed electronic state for all times. We have found in our applications that this correction step is generally unnecessary and the ensemble averaged results are unaffected if we leave it out, and it saves time. For our applications to I_2 in liquid xenon we find that the equations of motion can be accurately integrated with $\Delta = 0.25$ fs and $\delta = 0.01$ fs.

III. RESULTS

The results presented in this paper are meant to provide a survey of the different types of early time nonadiabatic relaxation dynamics that are available in solution after Frank–Condon photoexcitation of I_2 to its B state. Our aim at this point is not to reproduce the results of specific experiments but rather to provide a general overview of the effects of solvent on the nonadiabatic couplings between electronic states and to find out what types of relaxation pathways the calculations described here predict will be important in solution. The more ambitious task of computing specific experimental spectra will be the subject of a future publication.[117]

Our simulations were started from fcc lattices of 108 xenon atoms in which one of the atoms was replaced by an iodine molecule. Periodic boundary conditions were used. Ensembles of initial configurations at the various state points studied, each consisting of 48 members, were prepared from equilibrated configurations of the system sampled uniformly from long MD runs at the state points of interest using interaction potentials which approximate the DIM ground state accurately.[29,40] We report results for $T = 300$ K, at three different fluid densities $\rho^* = 0.3$, 0.7, and 1.0. Photoexcitation was initiated by abruptly changing the occupied state in each of the ensemble members from the ground state, $X, {}^1\Sigma_g^+$ to the excited state, $B, {}^3\Pi_u(0^+)$, leaving all coordinates and velocities unchanged. The evolution of the each ensemble member was monitored for 2 ps to explore the early time electronic relaxation. We find that typically the average temperature of our system increases by less than 10 K over the 2 ps after photoexcitation as the energy transfer from the intramolecular vibration to solvent thermal motions is slow on this timescale so heating of our finite sized system is not expected to be too significant. The smallest simulation box used in these studies has a cell dimension of $L \sim 20$ Å. All the interaction potentials used in these studies are short-ranged with characteristic lengthscales of about 4–5 Å, so finite size effects are small. The qualitative features of the results reported below are reproduced in ensembles with as few as 16 randomly selected members indicating that meaningful statistics are obtained from a sample with as few as ~ 50 trajectories.

Simply raising the ground state thermal distribution of trajectories up to the excited state as outlined above corresponds to irradiating with a broad band of frequencies which do not effect transitions to other electronic states. The distributions of excitation energies sampled by our thermal ensembles at the various densities are very broad (~ 0.5 eV or ~ 4000 cm^{-1}) compared to the typical linewidths of lasers used to photoexcite I_2 in experiments (the broadest lines used in ultrafast pulse experiments are only typically about 100–200 cm^{-1} wide). Our intent here, as mentioned above, is thus to probe all the different types of excitations possible in a single calculation to get an overview of the different relaxation channels made available by solvation.

We present our results in three subsections: (1) First, we survey the early time dynamics during which the I_2 bond extends on the excited B state surface and the thermal ensemble passes through various regions of interaction with other states. Our ensemble members sample a variety of different environments in which the electronic states are affected in different ways. Thus, the velocities with which different ensemble members encounter the various interaction regions, and the strengths of the couplings between the states for the ensemble members will all be different due to the effects of the unique solvation environment sampled by each ensemble member. Thus some trajectories may leave the initially prepared excited state very rapidly by coupling to other states, while other trajectories may remain in the B state for some time. (2) In the second subsection, we attempt to understand our very early time nonadiabatic electronic relaxation results in terms of the properties of the DIM Hamiltonian for the I_2-Xe cluster system thus attempting to address the issue of which nearest neighbor atoms in the solvent cage play the most important role inducing couplings between the states. (3) Finally we explore the longer term nonadiabatic dynamics, out to 2 ps, during which the separating atomic fragments begin to collide with the surrounding solvent molecules and thus start to lose their excitation energy. These early collisions with solvent will determine whether a molecule ultimately dissociates into atoms or, if the separating fragments can get rid of their energy quickly enough, the I_2 molecular bond may reform before the atoms lose each other, and are thermalized in the sea of solvent.

The results of our calculations presented below are displayed in the form of time histories of the state energies along typical individual trajectories. The instantaneously occupied state in these figures will be indicated by symbols. To help understand these energy records we also present the corresponding histories of the I_2 bond length for the various example trajectories.

A. Early time dynamics: Excited *B* state exit channels

At the lowest solvent density $\rho^* = 0.3$ we find that only about 30% of our trajectories leave the B state during the dynamics of the first bond extension. Increasing the solvent density makes this initial exit process more effective with about 70–75 % of trajectories leaving the B state on the first extension at the higher densities of $\rho^* = 0.7$ and $\rho^* = 1.0$.

We find that various channels are responsible for this

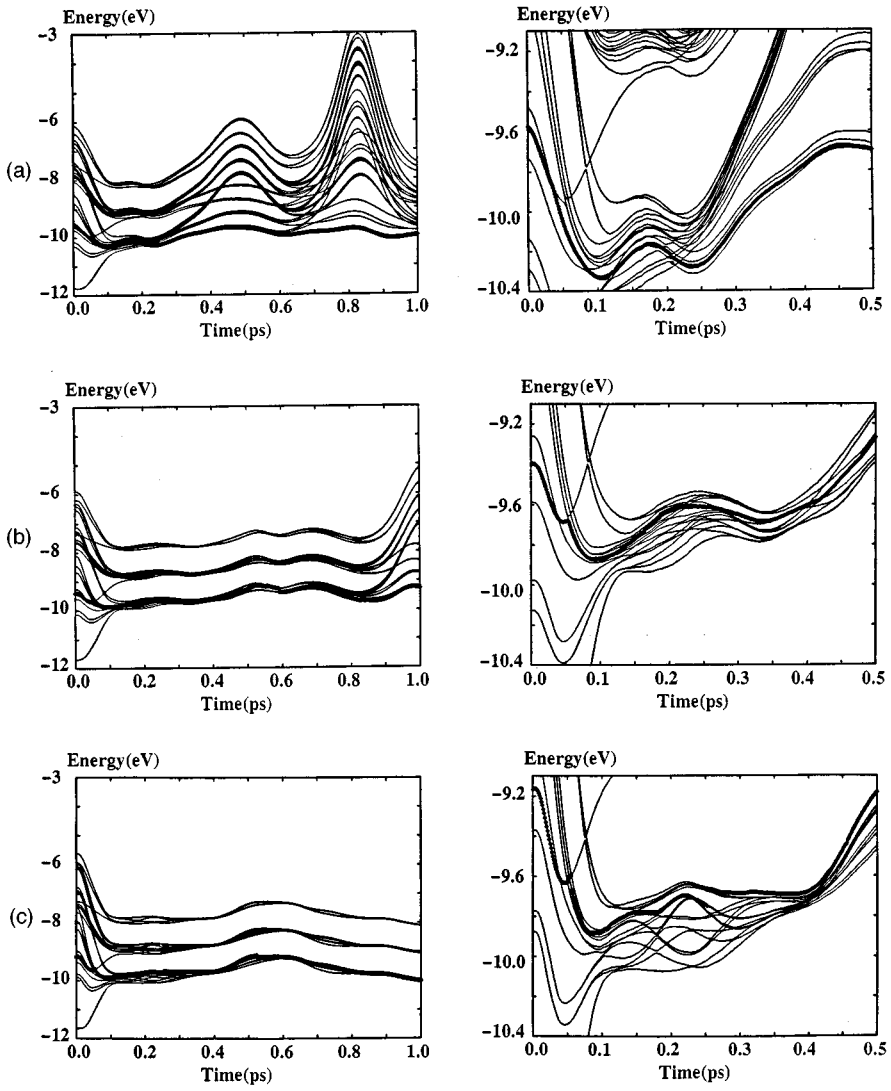

FIG. 5. Survey of principle channels used by trajectories which exit the B state on the first excited state bond extension and passage through the coupling region. Adiabatic eigenstate energies as functions of time are presented. The instantaneously occupied state is labelled with symbols. All trajectories shown are for a solvent density of $\rho^*=0.7$, but the same first passage exit channels are observed at other densities. Left column of panels gives full trajectories out to 1 ps, right column shows trajectories on expanded scales. The three principle first passage exit channels we find in solution are *via* the (a) $^1\Pi_u$, (b) $^3\Pi_{2g}$, and (c) a states.

initial B state exit process, and further, that the exit channels which are most important change with solvent density. The different types of initial exit channel dynamics which we find to be important in our calculations are surveyed in Fig. 5, where we plot trajectories from the $\rho^*=0.7$ ensemble which exhibit the different behaviors. Basically we find that there are only three important channels via which the initial B state exit takes place: (1) Exit through the $^1\Pi_u$ state [see Fig. 5(a)], i.e., the trajectory exits adiabatically as soon as it reaches the very first interaction region as the bond extends, (2) The trajectory moves diabatically at first, remaining in the B state as it hops straight through the $^1\Pi_u$ interaction region, then when it encounters the next interaction region with the $^3\Pi_{2g}$ state it undergoes adiabatic motion and exits the B state via this channel [see Fig. 5(b)], or (3) the trajectory stays in the B state till it reaches the a state where it exits adiabatically [see Fig. 5(c)]. Despite the fact that the B state intersects various other states at larger bond extensions, we have seen no examples, at any of the solvent densities studied, of trajectories leaving the B state through the a', $^3\Sigma_u^+(0^-)$, or $^3\Delta_{3u}$ states on the *first* initial rapid bond extension after excitation. These other states can play a role in electronically deactivating trajectories which stay in the B state for about a vibrational period or more as we shall see shortly.

As mentioned above, the relative importance of the $^1\Pi_u$, $^3\Pi_{2g}$, and a state channels for electronic relaxation on the first bond extension seems to vary some what with solvent density. At the lowest solvent density our statistics are not so good since only relatively few trajectories dissociate on the first extension at $\rho^*=0.3$. However, we find that the most important channel here is in fact the $^3\Pi_{2g}$ state, ac-

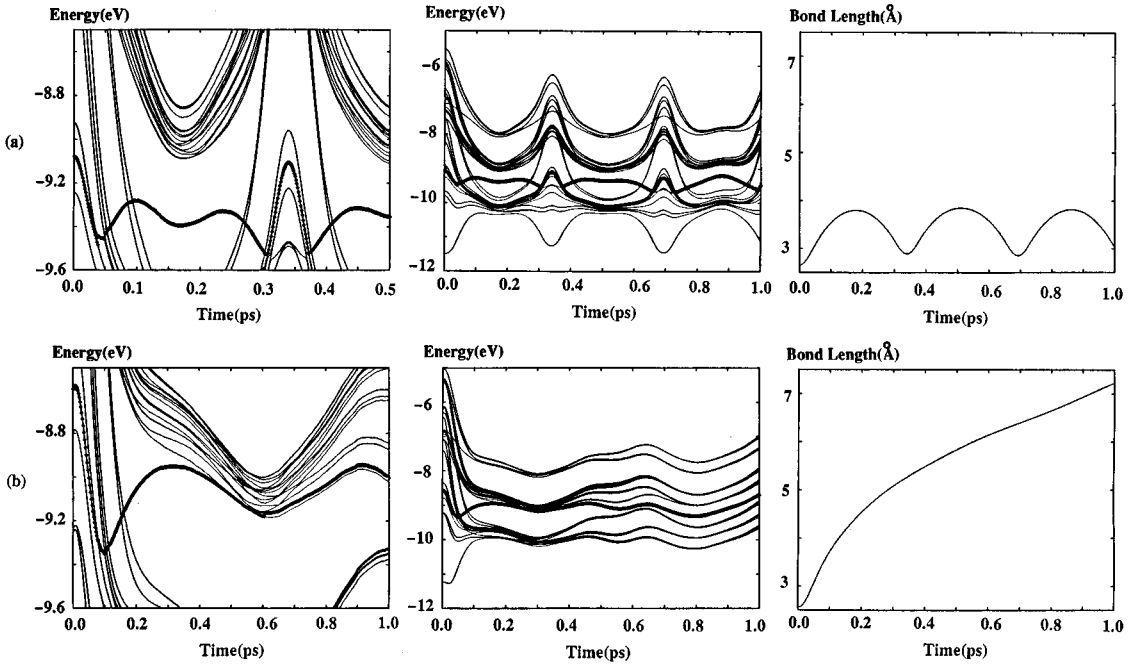

FIG. 6. Shows adiabatic state energy records for trajectories which do not exit the *B* state for 1 ps. Occupied state is labelled by symbols. Panels in row (a) show a typical trajectory which exhibits excited *B* state vibrational motion. Row (b) shows a trajectory which dissociates in the *B* state. Right hand column shows record of I−I bond length for these trajectories.

counting for roughly 60% of the first bond extension deactivations at $\rho^*=0.3$. Under these conditions, the $^1\Pi_u$, and *a* states each account for about 20% of the initial *B* state deactivations. As the solvent density is increased, however, the $^1\Pi_u$ state, i.e. the state first encountered as the bond extends, is found to become the dominant pathway, accounting for 60–70 % of the first bond extension *B* state deactivation processes. The less important $^3\Pi_{2g}$ and *a* channels account for the remaining 30–40 % of first bond extension deactivations in the high density range $\rho^*=0.7-1.0$, with the *a* state being the more important secondary channel under these conditions.

Various representative trajectories which initially move diabatically, and remain in the *B* state through the different interaction regions during the first bond extension are presented in Fig. 6. These types of trajectories either have sufficient kinetic energy in the I_2 bond to dissociate from the *B* state well and head off to start colliding with solvent atoms, or they are trapped in the *B* state well and, after reaching the outer turning points of their excited state motion they head back towards the various interaction regions where they will again attempt to exit from the *B* state. Excited state molecules which are effectively electronically decoupled from their environment may in principle undergo many excited *B* state vibrational periods as though they were in the gas phase.

Figure 6 shows example trajectories which exhibit these different types of phenomenon. Figure 6(a) shows a trajectory from our $\rho^*=0.7$ ensemble which exhibits several excited state vibrations. For the longer bond lengths in this example trajectory, the electronic system is always in the attractive *B* state but we see that it in fact feels repulsive forces at short bond extensions from several different electronic states; during the first period, it is repelled on the *B* state due to our initial preparation, the repulsive interactions during the second period arise from the *a* state, and those felt during the third period are associated with the $^1\Pi_u$ state. This intriguing behavior occurs due to strong electronic mixing between these states as the excited bond reforms. Figure 6(b) shows another trajectory from our $\rho^*=0.7$ ensemble which has very high kinetic in the I_2 bond and thus dissociates into the excited (3/2,1/2) atomic state manifold.

Figure 7 shows a variety of different trajectories which undergo *B* state electronic deactivation on either the inbound or outbound sections of their second period. At both $\rho^*=0.3$ and $\rho^*=0.7$, we see only the same deactivation channels open as we saw with the first bond extension, i.e., these delayed *B* state deactivation processes takes place via the $^1\Pi_u$, $^3\Pi_{2g}$, and *a* state channels. At the highest density, however, we see evidence of a new channel opening for these delayed deactivation processes. The example $\rho^*=1.0$ trajectory in Fig. 7(c) actually undergoes delayed deactivation through the $^3\Sigma_u^+(0^-)$ state.

B. Properties of the I_2-Xe molecular cluster DIM Hamiltonian

In an effort to address the question of which atoms in the nearest neighbor shell play the most import role inducing nonadiabtic couplings between the uncoupled I_2 gas phase diabatic potentials we have studied in detail the DIM Hamiltonian of the I_2-Xe molecular cluster.

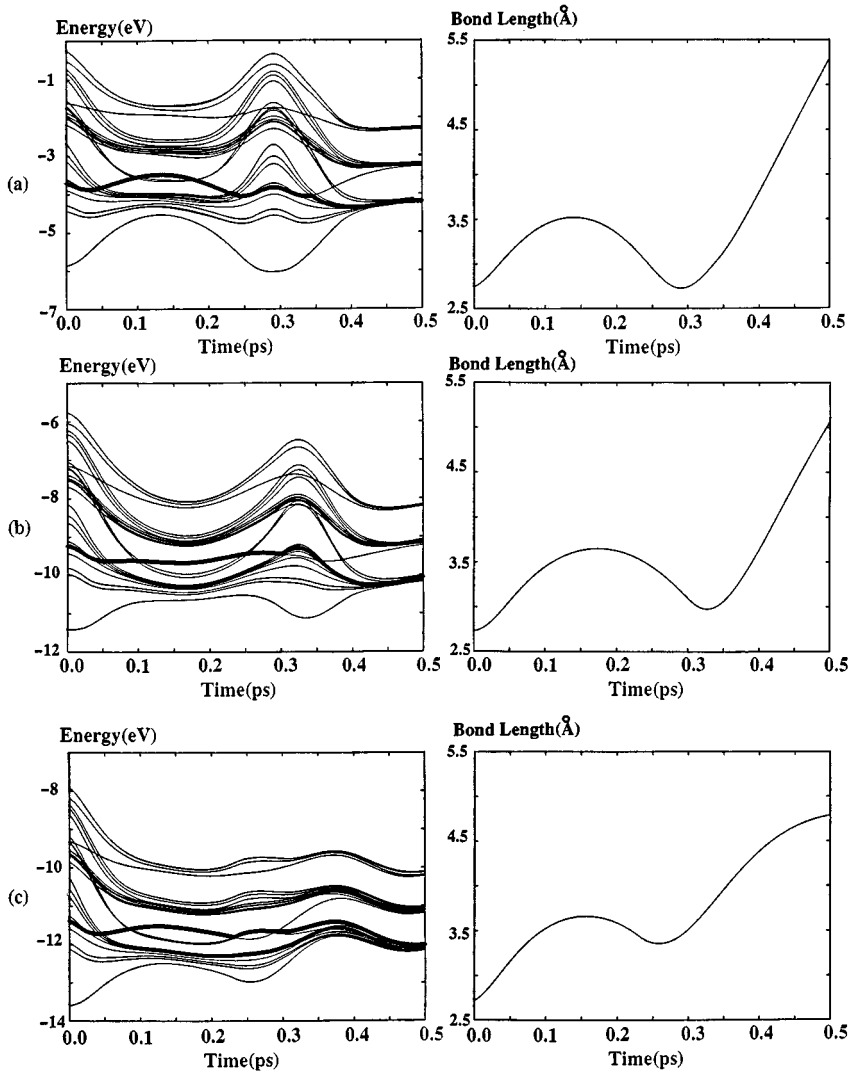

FIG. 7. Shows adiabatic state energy records with occupied state labelled with symbols for trajectories exiting B state on second passage through coupling region. At lower densities [$\rho^*=0.3$ (a) and $\rho^*=0.7$ (b)] same exit channels we found for first passage (Fig. 5) are observed. At higher densities [(c) $\rho^*=1.0$] we see the additional $^3\Sigma_u^+(0^-)$ channel become available.

In Figs. 8 and 9 we present various offdiagonal matrix elements of the DIM Hamiltonian for the I_2-Xe system which couple the B state [a state which dissociates to the excited (3/2,1/2) manifold of atomic states] to the manifold of states which dissociate to the ground (3/2,3/2) atomic state. In these figures we fix the I_2 bond length at 3 Å, in the middle of the coupling region between the B state and the states into which it undergoes predissociation. We plot the matrix elements as functions of $R_{I_2(\mathrm{com})-Xe}$ and θ, the angle between the $I-I$ bond and the $R_{I_2(\mathrm{com})-Xe}$ intermolecular vector.

Figure 8 gives the coupling matrix elements, obtained from our DIM calculations, between the B state and the set of lower lying states which are fairly well separated in energy from our excited state (see Fig. 1). Despite the fact that some of these couplings are quite large we generally find that the energy gaps from the B state to these lower states also remain large during the excited state dynamics presented in the previous subsection, so these lower lying levels generally do not play a role in the early time nonadiabatic electronic de-excitation of the B state. We see from Fig. 8(d), in fact, that the only state [the $^3\Pi_u(0^-)$] from this group of lower lying states which can get close in energy to the B state has vanishingly small coupling to it and is thus also not expected to play much of a role in initial B state electronic relaxation.

In Fig. 9, we plot the coupling matrix elements to the B state for the higher lying diabatic states which cross this state as the $I-I$ bond is extended. There are two important aspects of these coupling functions obtained from our DIM calculations on the I_2-Xe system: First, the only states which intersect the B state during the $I-I$ bond extension and also show appreciable values of coupling to the B state in some regions of I_2-Xe intermolecular configuration space are the $^1\Pi_u$, $^3\Pi_{2g}$, and a states [see Figs. 9(a)–9(c)]. Figs. 9(d)–9(f), on the other hand, indicate that there are no intermolecular geometries of the I_2-Xe system in which

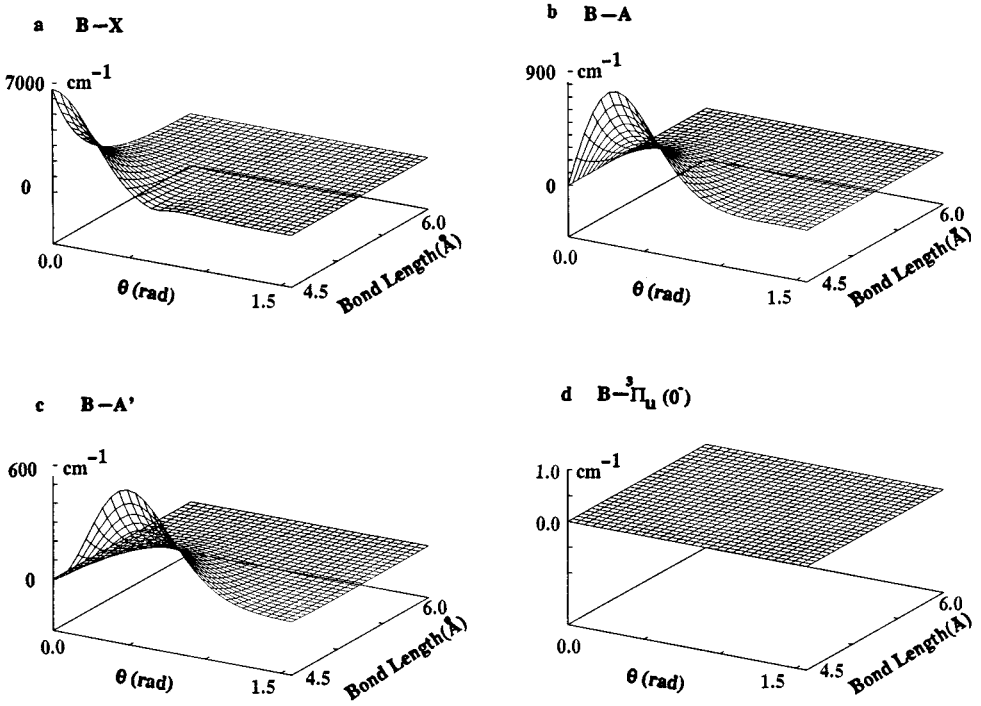

FIG. 8. DIM Hamiltonian matrix elements of the I_2-Xe cluster system for fixed $R_{I-I}=3$ Å, a characteristic separation in the middle of the coupling region between the B state and the important predissociative states. These Hamiltonian elements are displayed as a function of $R_{I_2(com)-Xe}$ bond length and relative orientation angle θ. Hamiltonian matrix elements coupling the B state to all states which dissociate to (3/2,3/2) atomic states which are always lower in energy than the B state are presented.

there are significant couplings between the B state and the a', $^3\Sigma_u^+(0^-)$, or $^3\Delta_{3u}$ states.

Secondly, we see that for these B intersecting states which do show strong couplings, the couplings themselves are fairly well localized in intermolecular configuration space. The couplings become quite small for I_2-Xe intermolecular distances beyond about 5 Å. Further, for solvent atom separations typical of the condensed phase, say 4–5 Å in this system, the region of strong coupling is localized over a fairly narrow range of small to intermediate angles, peaking at $\sim 15°$ for both the $B-{}^1\Pi_u$, and $B-a$ interactions and at $\sim 30°$ for the $B-{}^3\Pi_{2g}$ interaction.

The shapes and relative magnitudes of these offdiagonal coupling functions arise from the distance dependence of the $I-Xe$ diatomic fragment Hamiltonian elements we use in Eq. (2.6) together with the various subsequent orientational transformations summarized in Eqs. (2.7)–(2.12). We generally find that the basic trends in the coupling matrix elements and their magnitudes presented here vary only weakly with the $I-I$ bond length (2.5 Å$<R_{I-I}<4$ Å) for the typical range of intermolecular geometries explored here.

The early time nonadiabatic electronic relaxation dynamics summarized in the previous section can be understood almost entirely in terms of the I_2-Xe cluster Hamiltonian matrix elements presented here. As discussed above, the states of the I_2-Xe cluster with the largest offdiagonal Hamiltonian matrix elements which also intersect the B state as the $I-I$ bond length is extended are the $^1\Pi_u$, $^3\Pi_{2g}$, and a states. These are precisely the states which we have seen in the previous section provide the dominant electronically nonadiabatic relaxation channels for the B state in solution. The strength of the couplings between the states determined by these matrix elements can be thought of as the static component of the nonadiabatic mixing process. The other part of this process which results in the time varying mixed electronic state is the nuclear dynamical component which can be viewed as determining how long the different offdiagonal couplings each have to influence the dynamical mixed state. These two factors of course work in concert with one another to determine the mixed state dynamics.

The orientational dependence of the I_2-Xe coupling matrix elements we have seen here suggests that the atoms at small to intermediate angles, i.e., those cage atoms near the ends of the I_2 molecule play the most important role in the initial B state electronic deactivation. This reasoning from the cluster results assumes a pairwise additivity of the nonadiabatic effects. The Hamiltonian matrix is constructed in a pairwise additive fashion with in DIM but its diagonalization and the subsequent use of these eigenstates to describe the time dependent wave function makes the full nonadiabatic dynamics in reality a nonpairwise additive effect.

In the previous section, we found that at the highest density the new $^3\Sigma_u^+(0^-)$ channel for B state deactivation began to play a role. The fact that the I_2-Xe cluster Hamiltonian shows no coupling between the B and $^3\Sigma_u^+(0^-)$ states suggests that the opening of this deactivation channel at higher density arises due to the importance of many-body

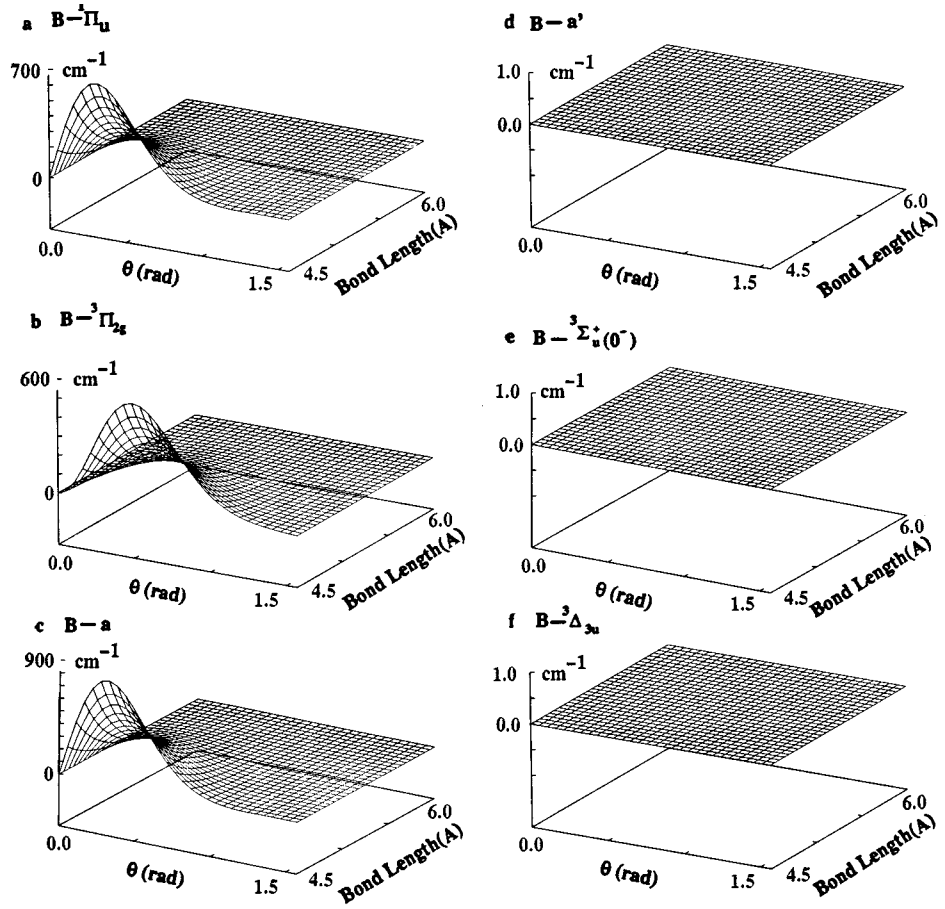

FIG. 9. Same as Fig. 8 except now coupling matrix elements between the B state and all states which dissociate to (3/2,3/2) atomic states and which also cross the B state at some value for R_{I-I} are displayed.

nonadiabatic interactions under these conditions. In many of the higher density trajectories displayed on expanded scales in the previous section, we see evidence of considerable gaps opening up between states which are uncoupled in our I_2-Xe cluster calculations. Many body complexes which occur in these higher density solutions can thus induce couplings between the B and a' or $^3\Sigma_u^+(0^-)$ as evidenced by the energy gaps opening between these states in Fig. 5 for example. The reason why relatively few of the trajectories in our ensembles have been observed to exit via these alternative channels is presumably because they require many body complexation and they lie at larger bond lengths than the other coupled states and, thus, the trajectory ensemble has more opportunity to exit through the channels it encounters first so exit channels nearest the turning points are statistically favored.

For completeness, the ground state potential surface predicted by our DIM calculations on the I_2-Xe cluster is presented in Fig. 10. In Fig. 10(a), we present a cut through this surface plotted in the same way as the coupling matrix elements described above, however, the I_2 bond length is held fixed at its equilibrium value in this figure. The figure indicates that the T-shaped geometry with $\theta=\pi/2$ has lower energy than the linear local minimum with $\theta=0$. Figure 10(b) shows cuts through this surface for these two orientations. The T-shaped global minimum, with a binding energy of around -460 K, allows the Xe atom to approach closer to the I_2 ($R_{I_2(com)-Xe}\sim 4.3$ Å) than in the linear local minimum ($R_{I_2(com)-Xe}\sim 5.6$ Å). Other rare gas-homonuclear halide clusters have also been found to show linear and T shaped minimum structures.[118]

C. Longer time dynamics: Early nonadiabatic collisions with surrounding solvent molecules

We have run our various ensembles out to 2 ps in an attempt to understand the longer time nonadiabatic dynamical processes which occur following photoexcitation and the early time electronic deactivation events discussed above. Our trajectories can be grouped into three different classes on the basis of the general characteristics of their longer time dynamics. Example trajectories from each of these three different classes are presented in Figs. 11–13. The energy level histories of our first class of trajectories presented in Fig. 11 are the easiest to understand. The broad distribution of energy levels of our I_2 molecule in xenon at zero time rapidly gives way to relatively narrow bands of perturbed atomic energy levels as the I atoms separate on the various dissociative states accessed when the I_2 leaves the B state via the mechanisms discussed in the previous subsection. The

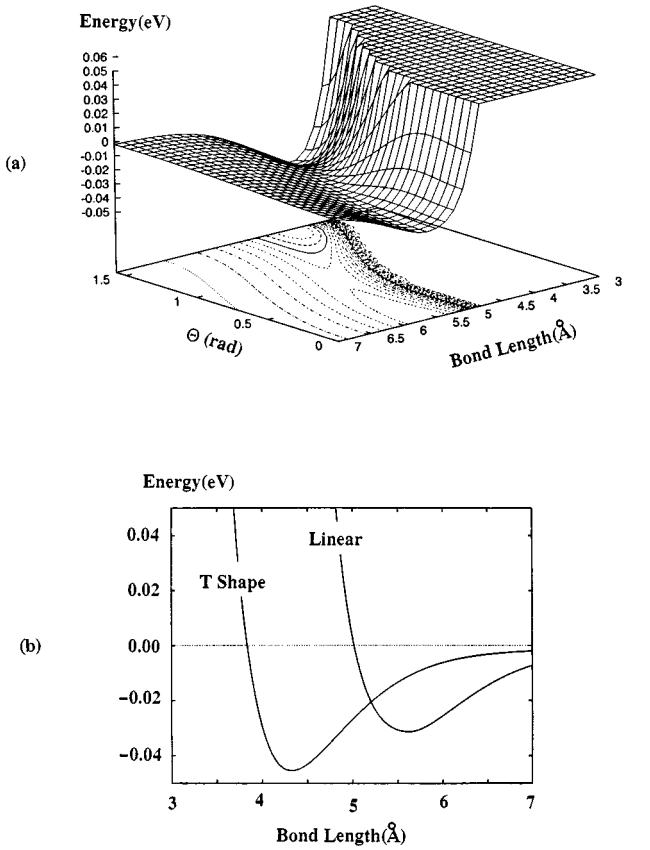

FIG. 10. (a) Ground state potential energy surface obtained from DIM calculations for I_2-Xe cluster system for R_{I-I} fixed at its gas phase equilibrium value displayed as a function of $R_{I_2(com)-Xe}$ bond length and relative orientation angle θ. (b) Cuts through this surface for linear and T-shaped cluster geometries.

widths of the atomic bands at longer times get broader as the density is increased. Fig. 11(b) shows the continuation of the trajectory presented in Fig. 7(c) which undergoes an excited state vibration before entering its dissociative state. For the trajectories displayed in Fig. 11, the two I atoms simply separate and undergo only very weak interactions with their surroundings for this 2 ps period. The number of trajectories which exhibit this type of behavior after dissociation is relatively insensitive to solvent density and we typically find these trajectories account for about 20–25 % of our ensemble.

The second class of longer time trajectories shows a richer energy level dynamics as seen in Fig. 12. Again, the I_2 molecular energy level pattern gives way to narrow bands of perturbed atomic levels with in 0.2 ps as the I atoms separate. Subsequently, in some trajectories [Fig. 12(c)] at higher densities, we see transient reformation of the I_2 molecular energy level pattern. In this case, the molecule vibrates briefly in the A state before the narrow band atomic energy level pattern appears once again. At about 1.5 ps in this trajectory the atomic levels suddenly begin to split up into different groups. This new characteristic energy level structure is in fact associated with the formation of unbound molecularlike energy levels associated with a collision between one of the I atoms and a Xe solvent atom. Our second group of trajectories all show the appearance of the energy level structures characterizing this $I-Xe$ collision complex. At low solvent densities ($\rho^*=0.3$) where some of our trajectories dissociate on the B state surface to the (3/2,1/2) excited state, these trajectories may be deactivated to the (3/2,3/2) ground state manifold by collisions with solvent atoms as we see in Fig. 12(a). At this lowest solvent density, the remaining 75% of trajectories all show this $I-Xe$ collision complex dynamics leading to separating atoms. At the higher solvent densities, only about 55–65% behave in this way.

At the highest density the remaining 20–25 % of our trajectories, typical examples of which are presented in Fig. 13, show evidence of molecular I_2 recombination. This behavior is *not* observed at the lowest density, and only seen in about 10% of trajectories from the $\rho^*=0.7$ ensemble. Again the broad band of I_2 molecular levels rapidly gives way to narrower atomic like bands as the I atoms separate. We then see evidence of $I-Xe$ collisions which again split up the atomic bands. After these $I-Xe$ collisions we see the reforming of I_2 molecular energy level structure. In these trajectories either, or both the I atoms have collided with their solvent cage and been brought back together to reform what appears to be a stable I_2 molecule. In all our example trajectories which display this type of behavior, the I_2 molecule reforms in the excited A' state. Solvent collisions have electronically and vibrationally de-excited the molecule sufficiently so that stable vibrational motion on the excited A' state now occurs.

IV. COMPARISONS WITH EXPERIMENT AND CONCLUSIONS

The results of the calculations reported in this paper on the early time electronically nonadiabatic relaxation after photoexcitation of I_2 to its B state in liquid xenon can be summerized as follows:

(1) The presence of the solvent induces couplings between the excited bound B state and various repulsive diabatic states which cross the B state as the I_2 bond extends. These couplings give rise to a variety of B state exit channels which lead to dissociation of the excited molecule. At higher solvent densities, exit from the B state and dissociation usually occurs on the first bond extension, generally in less than $\sim$100 fs, but can take several (1–3) excited state vibrational periods, extending the predissociation time out to $\sim$300 fs. The most important of these exit channels observed in our nonadiabatic MD calculations in solution coincide with states crossing the B state with the largest coupling matrix elements for the I_2-Xe cluster system. These cluster matrix elements are largest for solvent atom positions near the ends of the molecule. Our calculations predict that the $^1\Pi_u$ state plays the most important role in the dense solution phase electronically nonadiabatic relaxation of the excited B state. This is the first state encountered as the I_2 bond is extended. Other states with appreciable B state coupling matrix elements in the I_2-Xe cluster which also participate in B state

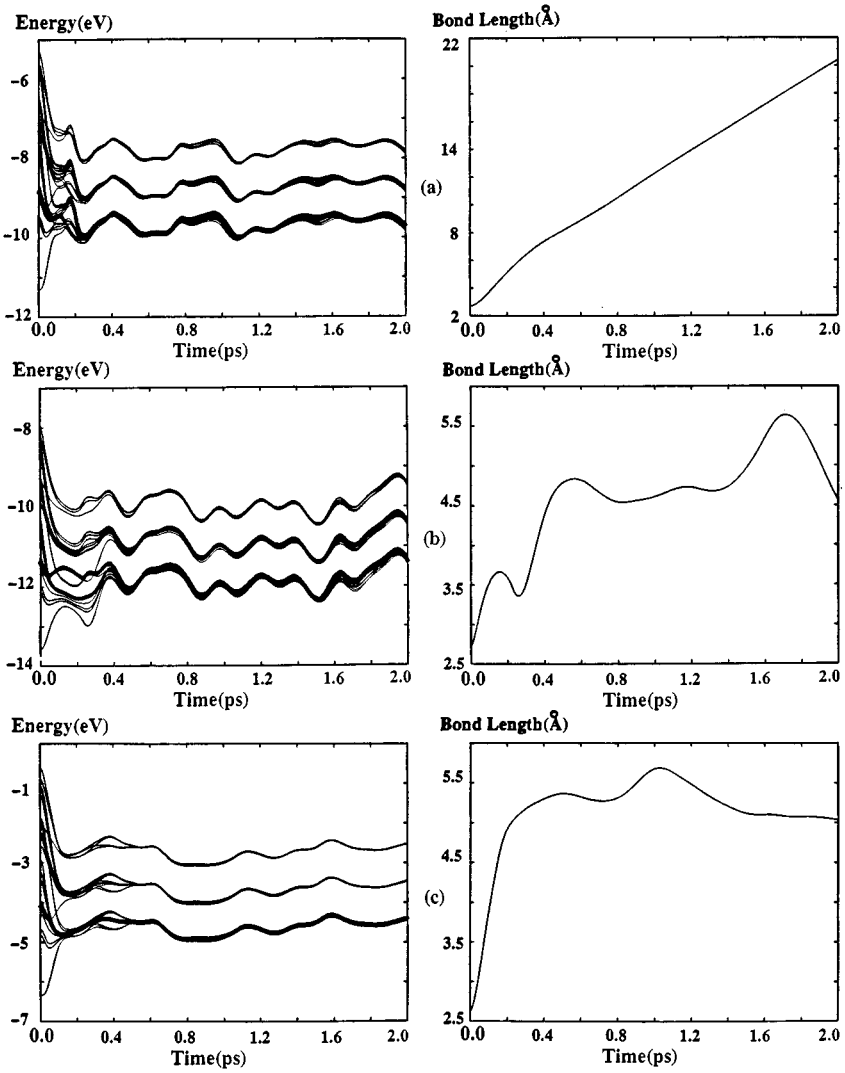

FIG. 11. Adiabatic state energy records with occupied state labelled with symbols for longer time trajectories which dissociate to two separating ground state iodine atoms which do not undergo strong solvent collisions with in 2 ps. Typical trajectories exhibiting this behavior at different densities (a) $\rho^*=0.7$, (b) $\rho^*=1.0$, and (c) $\rho^*=0.3$ are presented.

electronic relaxation in solution include the $^3\Pi_{2g}$ and *a* state channels to dissociation. At the highest solvent density ($\rho^*=1.0$), states which show no *B* state coupling in the I_2-Xe cluster, such as the $^3\Sigma_u^+(0^-)$, can begin to play a role in *B* state de-excitation through the establishment of many-body interaction complexes.

(2) The main results of our longer time dynamical studies are that at lower solvent densities ($\rho^*=0.3$) the separating I atom fragments resulting from the initial photoexcitation and *B* state predissociation can collide with solvent atoms and be de-excited. Generally, at these low densities, however, we find no evidence of I_2 recombination with in the first 2 ps. Under these low density conditions the I atoms can escape from the molecule's solvent cage and the individual I atoms move free from one another undergoing independent collisions with solvent atoms. However, at higher solvent densities ($\rho^*=0.7$, and especially at $\rho^*=1.0$), we start to see I_2 geminate recombination processes taking place with in the first 1.0–2 ps. These processes result from solvent collisional deactivation of the I atom fragments. All our trajectories which exhibit the reformation of the I_2 bond do so after only 1 or 2 solvent atom collisions which usually leave the recombined, vibrationally hot molecule in the excited A' state.

The qualitative agreement between the findings of our calculations summarized above and the results of various experiments on I_2 predissociation and geminate recombination is remarkably good.

An enormous body of experimental work on I_2 photodissociation, geminate recombination, and subsequent vibrational relaxation in solution has been developed since the 1930's[9,12,21,23,24,119–121] (the review by Harris *et al.*[1] provides an excellent summary of this field and the important timescales of the problem).

The correct timescales for both predissociation and geminate recombination of I_2 in CCl_4 solution were first

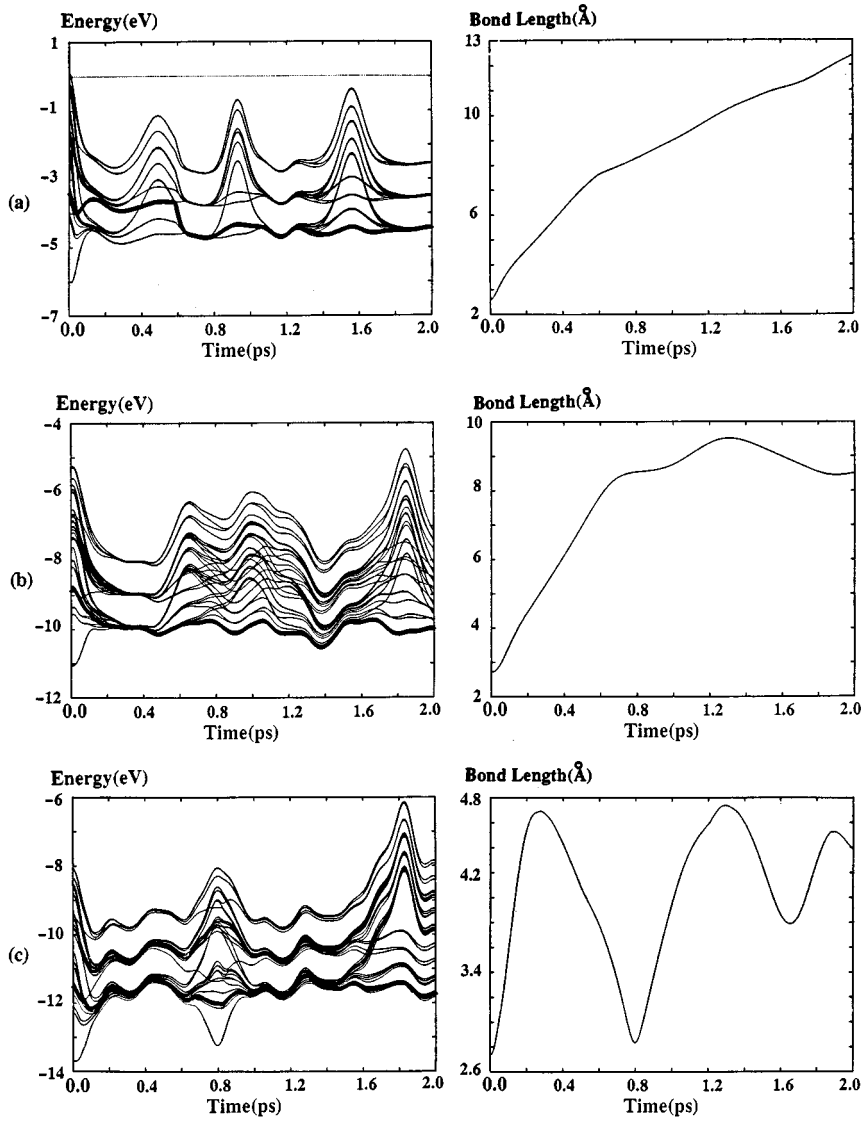

FIG. 12. Adiabatic state energy records with occupied state labelled with symbols for longer time trajectories which dissociate to two separating ground state iodine atoms which undergo strong solvent collisions with in 2 ps. (a) Shows a $\rho^*=0.3$ trajectory which initially dissociates in the excited (3/2,1/2) atomic state manifold and a strong solvent collision subsequently pushes it into the (3/2,3/2) ground state manifold. (b) presents a $\rho^*=0.7$ trajectory in which the two separating ground state I atoms both undergo strong collisions with surrounding Xe solvent molecules. (c) In this trajectory at $\rho^*=1.0$ the dissociating I atoms collide with the solvent cage and exhibit a transient recombination in the excited A state. They subsequently dissociate and undergo strong solvent collisions.

identified in the late 1980's in picosecond experiments by Smith and Harris.[10] Their findings were that predissociation was much more rapid than the 10–15 ps indicated by previous studies[9,121] and in fact took place in less than 1 ps or with in a few collision times in agreement with early gas phase work in xenon.[6,122] Further, these solution phase studies put an upper bound on the timescale for geminate recombination to form highly vibrationally excited I_2 molecules in their X or A' states which also occurred very rapidly in less than 2 ps. These general timescales for both predissociation and geminate recombination are of course in excellent agreement with the timescales we find in our calculations at higher densities. The reduced density of CCl_4 under normal conditions is $\rho^*=0.9135$ so our calculations predict that geminate recombination to the A' state should be observed in less than 2 ps. Recombination to the A' state has been observed experimentally by a number of groups in various solvent environments.[9,10,15,18,19]

Very recently, however, direct femtosecond time resolved studies of the I_2 predissociation process in the condensed phase have been conducted,[7,8] as well as, analysis of the resonance Raman overtone progressions of I_2 in various liquids[123,124] which also yield information, in an indirect fashion, on the femtosecond timescale predissociation dynamics. Ever since it became apparent that the B state was intersected by more than one dissociative state, the precise channel for predissociation has been a controversial issue, and despite the remarkable time resolution now available in experiments this continues to be the case.

Scherer *et al.*, working with I_2 in liquid n-hexane, mea-

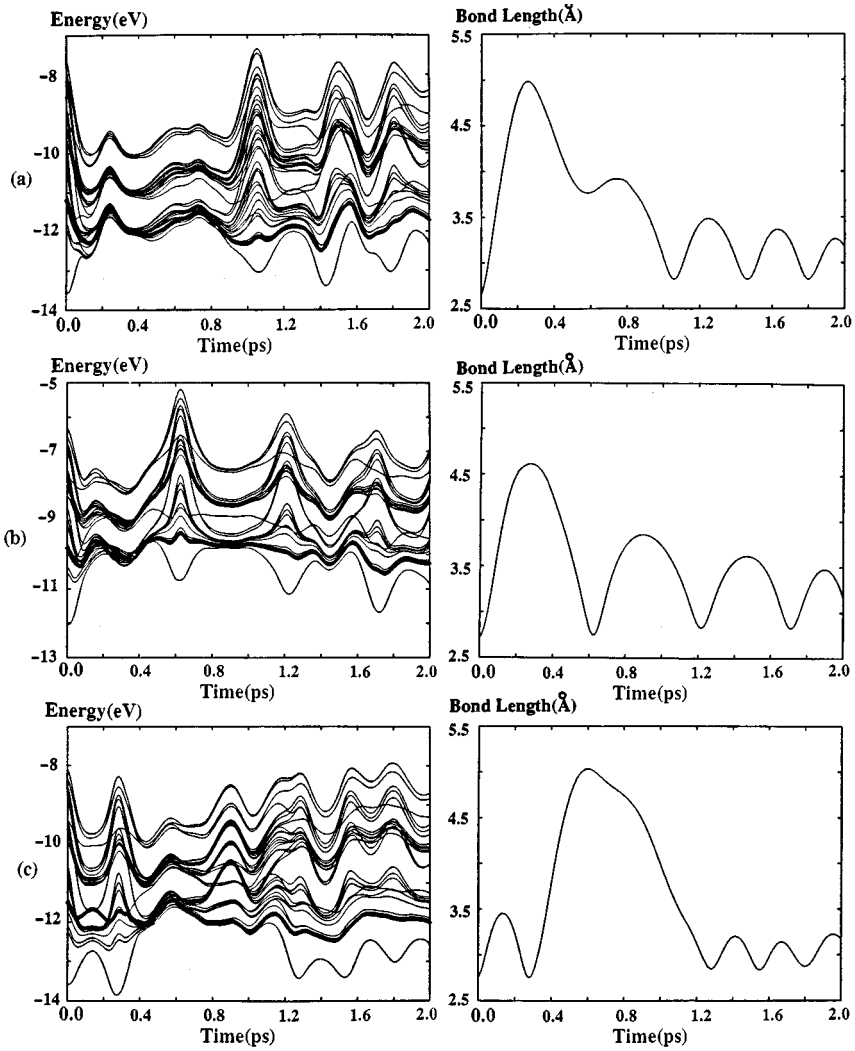

FIG. 13. Adiabatic state energy records with occupied state labelled with symbols for three different trajectories from our $\rho^* = 1.0$ ensemble which all exhibit geminate recombination of the I_2 molecule in its excited A' state after dissociating iodine atoms collide with solvent molecules.

sure the transient dichroic response in two color experiments, fixing the pump wavelength at 580 nm and varying the probe over the range 640–460 nm. They fit their data to a sum of damped oscillatory terms, each of which they interpret as a signal arising from a nuclear wave packet moving over a different electronic surface. The frequencies of the nuclear vibrations on the different electronic surfaces can thus be obtained directly from these fits, and the fitted phase angles give information about when the motion on the various surfaces began.

The 580 nm pump takes molecules from their X ground state to below the gas phase dissociation limit of the B state at a bond length of about 2.8 Å according to the classical Franck principle, which places the excited molecules on the inner repulsive wall of the B state potential (see Fig. 1). Oscillation of the nuclear wave packet over the excited B state surface causes it to pass through the various interaction regions releasing density onto the different dissociative surfaces coupled to this state every B state vibrational period. The probe field takes excited state molecules up to some other excited electronic state believed to be a solvated ion-pair state of I_2. The different probe frequencies define various bond length windows depending on how the difference potential between the currently occupied state and the excited ion-pair state vary. By monitoring the time delay for probe absorption of a particular wavelength they can thus time how long it takes the packet to get to a particular bond length. The longest probe wavelengths correspond to exciting the packet while it is still in the B state (640–526 nm), and shorter wavelengths (510–460 nm) are required to excite the packet once it has crossed over to a predissociative repulsive surface.

There are two important findings from these experiments: (1) Probe absorptions from the predissociative states are first observed at a delay time of 150 fs after photoexcitation, and (2) predissociative state absorptions to the ion-pair state are typically about 10 times more intense than B state absorptions presumably terminating in the same ion-

pair state. These experiments thus indicate that in the condensed phase excited B state I_2 molecules are able to couple onto a dissociative state (or states) with in half a B state vibrational period of photoexcitation. The fact that the absorption intensity from the dissociative states to the upper ion pair state is considerably larger than similar absorptions by the B state gives a clue as to the possible identities of these dissociative states.

The 150 fs time scale for observing absorption from predissociative states obtained from these experiments is completely consistent with the results of our calculations at the higher solvent densities. By 100–150 fs all our initial B state trajectories have traversed the interaction regions of all the states intersecting the B state. Our very earliest B state departures occur via the $^1\Pi_u$ state with in 30–50 fs. Departures via the a or $^3\Pi_{2g}$ states typically occur around 50 fs.

The classical treatment of the I_2 bond extension, basic to our approach, generally predicts that changes occur more abruptly than for the true quantum dynamical motion of a more delocalized wave packet. The classical trajectories make transitions only when they reach the interaction regions while more diffuse wave packets can continue to allow probability flux onto a coupled surface, even when the mean packet position is some distance from the coupling region, depending on the spatial extent of the packet. Thus the true quantal description of the nonadiabatic transition should be smeared out in time and space relative to our surface hopping trajectory representation. This smearing may have some effect on the mean time of transition if the coupling region is asymmetrical. We believe however that an estimate of 30–70 fs for the delay time to cross over to the dissociative surfaces based on our calculations is reasonable. Improved experimental resolution in these pump–probe femtosecond experiments would be necessary if such short times are to be confirmed from these experiments.

The results of Scherer and co-workers do not give any direct experimental evidence as to precisely which state or states are involved in the B state predissociation dynamics. Their results are simply consistent with these states being more strongly dipole coupled to the proposed upper ion pair state than the B state. In their discussion, these authors favor the a or a' states as being the most likely channels for predissociation in solution and suggest that the $^1\Pi_u$ does not play much of a role in predissociation. This speculation is based on qualitative guesses about the intensities of transitions from the a or a' states to a possible ion-pair excited state based on findings from early qualitative studies of gas phase I_2 states by Mulliken.[112] In addition, they present arguments based on circumstantial evidence, as well as, the findings of beam experiments[118] on the ''one atom cage effect'' to support their speculation. These beam experiments probe the importance of $X \rightarrow B$ versus $X \rightarrow {}^1\Pi_u$ transitions for photoexcitation and have nothing to do with the strength of $B-{}^1\Pi_u$ couplings induced by the presence of a solvent atom.

The starting point for their proposal that the $^1\Pi_u$ state is unimportant for predissociation compared to the a state goes back to the symmetry arguments of Tellinghuisen[125] concerning the relative sizes of the couplings responsible for electric versus magnetic field predissociation of I_2. These perturbation theory arguments apply in weak, isotropic, uniform fields. Recent speculation on the symmetry breaking nature of fields around atoms, and in solution[126] have raised questions about the usefulness of such uniform field perturbation theory results for solution phase anisotropic environments. Our I_2-Xe cluster results indeed give zero $B-{}^1\Pi_u$ couplings for the highly symmetric situations of parallel and perpendicular orientation but, for less symmetric geometries, we find appreciable couplings.

The recent analysis of vibrational overtone intensities from resonance Raman studies of I_2 in liquid xenon[123,124] favors the $^1\Pi_u$ predissociation channel in agreement with the results of our calculations. In these experiments Chergui and co-workers measure the integrated intensities of vibrational overtones for different excitation wavelengths. They interpret their results in terms of excited state wave packet time correlation functions as described by Heller and co-workers.[127] As the initially excited wave packet moves over the B state surface it radiates down to the ground electronic state picking out different ground state vibrational levels depending on the excited state wavepacket's time dependent B state vibrational level composition, and the size of the Franck–Condon factors for transitions between upper and lower electronic state vibrational levels.

At short excitation wavelength ($\lambda < 520$ nm), corresponding to sufficient energy in the I_2 vibrational coordinate to diabatically dissociate the B state bond, they see the overtone intensity decay rapidly with vibrational quantum number. The initially excited state wave packet thus spends relatively little time in upper state vibrational levels with appreciable overlap with ground state levels, other than the lowest levels from which it was created, before the packet leaves the B state well and dissociates. At $\lambda = 520$ nm an abrupt change in the overtone intensity distribution is observed associated with the preparation of a highly vibrationally excited wave packet which exhibits bound oscillatory motion just below the B state dissociation threshold. This highly excited bound wave packet samples upper state vibrational levels with appreciable Franck–Condon overlap with a wide spectrum of ground state levels giving a broad distribution of overtone intensities. The early sudden drop in intensity from overtone 2 to overtone 3 before the broad intensity distribution for higher overtones at $\lambda = 520$ nm is associated with some predissociation of this highly vibrationally excited packet.

As the excitation wavelength is increased and the initial excited state wave packet is prepared in superpositions dominated by lower vibrational levels on the upper surface, the broad distribution of integrated overtone intensities gives way to distributions which decay more rapidly with overtone number, but they all show sudden early drops in intensity. The relative size of this sudden drop in overtone intensity at low overtone number gets larger at longer wavelengths, exciting lower into the upper state vibrational manifold.

These authors argue that the strong drops in intensity at distinct overtones indicate that the predissociation occurs

near the turning points of these overtones and the size of the intensity drop is related to the probability of hopping to the predissociative state. They see the largest intensity drop due to this predissociation occur for $\lambda = 590$ nm excitation where the drop takes place for overtones corresponding to $v'' = 2-5$. The classical turning points for these states are close to bondlengths of $R_{I-I} \sim 2.87$ Å indicating approximately the region of the B state crossing to the predissociative state. Frank–Condon excitation at $\lambda = 590$ nm puts the wave packet at ~ 2.8 Å initially, and they thus estimate that classically it takes about 25 fs for this packet to reach the crossing point with this excitation wavelength. For $\lambda = 520$ nm excitation, mentioned above, the weaker intensity drop (higher velocity gives lower Landau–Zener probability of hopping to the predissociative state) occurs in a similar overtone range ($v'' = 2-3$). This packet starts at ~ 2.65 Å and classically takes about 35 fs to reach the crossing point for predissociation. These workers suggest that this positioning of the crossing point makes it more likely that the dominant channel for predissociation is the $^1\Pi_u$ state, consistent with the findings of our calculations. These authors argue further that their data at $\lambda = 520$ nm suggests that the overtone intensity distribution shows a second drop corresponding to $v'' \sim 9$ which they associate with predissociation through a second channel, suggesting either the a or a' states. Our observation of a or $^3\Pi_{2g}$ predissociation is also consistent with this interpretation of their data.

The ability of nonadiabatic MD methods coupled with semiempirical excited state electronic structure techniques to semiquantatively reproduce experimental trends in ultrafast photoexcited dynamics as demonstrated in this paper indicates the enormous potential of this computational methodology for exploring excited state chemistry in solution. The accuracy and applicability of nonadiabatic MD methods is reasonably well understood and recent developments in these methods are aimed at including quantal nuclear effects through semiclassical techniques.[76,77] Our ability to extend the general scheme used in this paper to more complex systems really hinges on the availability of accurate ground and excited state diatomic interaction potentials, and the applicability of the approximations underlying the DIM semiempirical electronic structure methods. Spectroscopic and scattering measurements of the fragment surfaces are becoming more widely available, and *ab initio* electronic structure calculations on the excited states of diatomic fragments can also provide reliable results. Future studies of the applicability of these methods to the photoexcited dynamics of polyatomics and charged systems in solution where there is much detailed experimental work will be useful to explore the generality of these methods.

ACKNOWLEDGMENTS

We gratefully acknowledge financial support for this work from the National Science Foundation (Grant Nos. CHE-9058348 and CHE-9521793), and the Petroleum Research Fund administered by the American Chemical Society (Grant No. 27995-AC6), and a generous allocation of supercomputer time from the National Center for Supercomputing Applications. D.F.C. also acknowledges financial support from CECAM, and the hospitality of G. Ciccotti, and S. Baroni during his sabbatical visit. D.F.C. is a Presidential Young Investigator.

[1] A.L. Harris, J.K. Brown, and C.B. Harris, Annu. Rev. Chem. **39**, 341 (1988).
[2] R. M. Bowman, M. Dantus, and A. H. Zewail, Chem. Phys. Lett. **161**, 297 (1989).
[3] M. Dantus, R. M. Bowman, and A. H. Zewail, Nature **343**, 737 (1990).
[4] M. Grubele, G. Roberts, M. Dantus, R. M. Bowman, and A. H. Zewail, Chem. Phys. Lett. **166**, 321 (1990).
[5] M. Grubele and A. H. Zewail, J. Chem. Phys. **98**, 894 (1993).
[6] G.A. Capelle and H.P. Broida, J. Chem. Phys. **58**, 4212 (1973).
[7] N. F. Scherer, D. M. Jonas, and G. R. Fleming, J. Chem. Phys. **99**, 153 (1993).
[8] N.F. Scherer, L.D. Ziegler, and G.R. Fleming, J. Chem. Phys. **96**, 5544 (1992).
[9] A.L. Harris, M. Berg, and C.B. Harris, J. Chem. Phys. **84**, 788 (1986).
[10] D.E. Smith and C.B. Harris, J. Chem. Phys. **87**, 2709 (1987).
[11] M.E. Paige and C.B. Harris, Chem. Phys. **149**, 37 (1990).
[12] D.F. Kelly, N.A. Abul-Haj, and D.J. Jang, J. Chem. Phys. **80**, 4105 (1984).
[13] N.A. Abul-Haj and D.F. Kelly, J. Chem. Phys. **84**, 1335 (1986).
[14] N.A. Abul-Haj and D.F. Kelly, Chem. Phys. Lett. **119**, 182 (1985).
[15] C. Lienau and A.H. Zewail, J. Chim. Phys. **92**, 566 (1995).
[16] E.D. Potter, Q. Liu, and A.H. Zewail, Chem. Phys. Lett. **200**, 605 (1992).
[17] Q. Liu, J.K. Wang, and A.H. Zewail, Nature **364**, 427 (1993).
[18] C. Lienau, J.C. Williamson, and A.H. Zewail, Chem. Phys. Lett. **213**, 289 (1993).
[19] C. Lienau and A.H. Zewail, Chem. Phys. Lett. **218**, 224 (1994).
[20] M.E. Paige and C.B. Harris, J. Chem. Phys. **93**, 1481 (1990).
[21] X. Xu, S. Yu, R. Lingle, H. Zhu, and J.B. Hopkins, J. Chem. Phys. **95**, 2445 (1991).
[22] D. Nesbitt and J.T. Hynes, J. Chem. Phys. **77**, 2130 (1982).
[23] P. Bado, C. Dupuy, D. Magde, K.R. Wilson, and M.M. Malloy, J. Chem. Phys. **80**, 5531 (1984).
[24] P. Bado and K.R. Wilson, J. Phys. Chem. **88**, 655 (1984).
[25] A.H. Lipkus, F.P. Buff, and M.G. Sceats, J. Phys. Chem. **79**, 4830 (1983).
[26] C.L. Brooks and S.A. Adelman, J. Phys. Chem. **80**, 5598 (1984).
[27] R.H. Stote and S.A. Adelman, J. Phys. Chem. **88**, 4415 (1988).
[28] D.J. Russell and C.B. Harris, Chem. Phys. **183**, 325 (1994).
[29] J.K. Brown, C.B. Harris, and J.C. Tully, J. Chem. Phys. **89**, 6687 (1988).
[30] J.K. Brown, D.J. Russell, D.E. Smith, and C.B. Harris, Phys. Rev. Appl. **22**, 1787 (1987).
[31] D.L. Bunker and B.S. Jacobson, J. Am. Chem. Soc. **94**, 1843 (1972).
[32] J.N. Murrell, A.J. Stace, and R. Dammell, J. Chem. Soc. Faraday Trans. **274**, 1532 (1978).
[33] J.T. Hynes, R. Kapral, and G.M. Torrie, J. Chem. Phys. **72**, 177 (1980).
[34] M. Schell and R. Kapral, Chem. Phys. Lett. **81**, 83 (1981).
[35] B. Martire and R.G. Gilbert, Chem. Phys. **56**, 241 (1981).
[36] D.P. Ali and W.H. Miller, J. Chem. Phys. **78**, 6640 (1983).
[37] D.P. Ali and W.H. Miller, Chem. Phys. Lett. **105**, 501 (1984).
[38] J.M. Dawes and M.G. Sceats, Chem. Phys. **96**, 315 (1985).
[39] M.G. Sceats, Chem. Phys. **96**, 299 (1985).
[40] W. Wang, K.A. Nelson, L. Xiao, and D.F. Coker, J. Chem. Phys. **101**, 9663 (1994).
[41] J.C. Tully and R.K. Preston, J. Chem. Phys. **55**, 562 (1971).
[42] J.C. Tully, in *Dynamics on Molecular Collisions, Part B*, edited by W. H. Miller (Plenum, New York, 1976), p. 217.
[43] J.C. Tully, J. Chem. Phys. **93**, 1061 (1990).
[44] J.C. Tully, Int. J. Quant. Chem. **25**, 299 (1991).
[45] S. Hammes-Schiffer and J.C. Tully, J. Chem. Phys. **101**, 4657 (1994).
[46] S. Hammes-Schiffer and J.C. Tully, J. Chem. Phys. **103**, 8528 (1995).
[47] F. Webster, P.J. Rossky, and R.A. Friesner, Comp. Phys. Comm. **63**, 494 (1991).
[48] F.J. Webster, E.T. Tang, P.J. Rossky, and R.A. Friesner, J. Chem. Phys. **100**, 4835 (1994).
[49] P.J. Kuntz, J. Chem. Phys. **95**, 141 (1991).
[50] P.J. Kuntz and J.J. Hogreve, J. Chem. Phys. **95**, 156 (1991).

[51] R. E. Cline and P. G. Wolynes, J. Chem. Phys. **86**, 3836 (1987).
[52] J. R. Stine and J. T. Muckerman, J. Phys. Chem. **91**, 459 (1987).
[53] J. R. Stine and J. T. Muckerman, J. Chem. Phys. **65**, 3975 (1976).
[54] J. R. Stine and J. T. Muckerman, J. Chem. Phys. **68**, 185 (1978).
[55] N. C. Blais and D. G. Truhlar, J. Chem. Phys. **79**, 1334 (1983).
[56] N. C. Blais, D. G. Truhlar, and C. A. Mead, J. Chem. Phys. **89**, 6204 (1988).
[57] W.H. Miller and F.F. George, J. Chem. Phys. **56**, 5637 (1972).
[58] A. Warshel, J. Phys. Chem. **86**, 2218 (1982).
[59] A. Warshel and J-K. Hwang, J. Chem. Phys. **84**, 4938 (1986).
[60] A. Warshel and J-K. Hwang, J. Chem. Phys. **82**, 1756 (1985).
[61] A. Warshel and W.W. Parson, Ann. Rev. Phys. Chem. **42**, 279 (1991).
[62] D. Thirumalai, E.J. Bruskin, and B.J. Berne, J. Chem. Phys. **83**, 230 (1985).
[63] M. F. Herman and E. Kluk, in *Dynamical Processes in Condensed Matter*, edited by M. W. Evans (Wiley, New York, 1985), p. 577.
[64] M. F. Herman, J. Chem. Phys. **81**, 754 (1984).
[65] M. F. Herman, J. Chem. Phys. **81**, 764 (1984).
[66] M. F. Herman, J. Chem. Phys. **87**, 4779 (1987).
[67] M. F. Herman, J. Chem. Phys. **103**, 8081 (1995).
[68] D.F. Coker, in *Computer Simulation in Chemical Physics*, edited by M. P. Allen and D. J. Tildesley (Kluwer Academic, Dordrecht, 1993), pp. 315–377.
[69] D.F. Coker and L. Xiao, J. Chem. Phys. **102**, 496 (1995).
[70] H.S. Mei and D.F. Coker, J. Chem. Phys. **104**, 4755 (1996).
[71] M. Ben-Num, R.D. Levine, D.M. Jonas, and G.R. Flemming Chem. Phys. Lett. **245**, 629 (1995).
[72] M. Ben-Num and R.D. Levine, Chem. Phys. **201**, 163 (1995).
[73] M. Ben-Num, R.D. Levine, and G.R. Fleming (preprint).
[74] Z. Li, J.Y. Fang, and C.C. Martens, J. Chem. Phys. **104**, 6919 (1996).
[75] T.H. Murphrey and P.J. Rossky, J. Chem. Phys. **103**, 6665 (1995).
[76] E.R. Bittner and P.J. Rossky, J. Chem. Phys. **103**, 8130 (1995).
[77] E. Neria and A. Nitzan, J. Chem. Phys. **99**, 1109 (1993).
[78] I.H. Gersonde and H. Gabriel, J. Chem. Phys. **98**, 2094 (1993).
[79] A.I. Krylov, R.B. Gerber, and V.A. Apkarian, Phys. Chem. **189**, 261 (1994).
[80] A.I. Krylov and R.B. Gerber, Chem. Phys. Lett. **231**, 395 (1994).
[81] W.G. Lawrence and V.A. Apkarian, J. Chem. Phys. **101**, 1820 (1994).
[82] R. Zadoyan, Z. Li, C.C. Martens, and V.A. Apkarian, J. Chem. Phys. **101**, 6648 (1994).
[83] R. Zadoyan, Z. Li, P. Ashjian, C.C. Martens, and V.A. Apkarian, Chem. Phys. Lett. **218**, 504 (1994).
[84] J. Zoval and V.A. Apkarian, J. Phys. Chem. **98**, 7945 (1994).
[85] Z. Li, R. Zadoyan, V.A. Apkarian, and C.C. Martens, J. Phys. Chem. **99**, 7453 (1995).
[86] R. Zadoyan, Z. Li, C.C. Martens, and V.A. Apkarian, in *Laser Techniques for State-Selected and State-to-State Chemistry II*, edited by J. W. Hepburn, SPIE Proceedings, 1994, p. 233.
[87] R. Zadoyan, Z. Li, O. Ashjian, C.C. Martens, and V.A. Apkarian, *Ultrafast Phenomena, Vol. 7* (Springer Verlag, New York, 1994).
[88] F.O. Ellison, J. Am. Chem. Soc. **85**, 3540 (1963).
[89] F.O. Ellison and J.C. Patel, J. Am. Chem. Soc. **85**, 3544 (1963).
[90] F.O. Ellison and J.C. Patel, J. Am. Chem. Soc. **86**, 2115 (1963).
[91] A. Warshel and R.M. Weiss, J. Am. Chem. Soc. **102**, 6218 (1980).
[92] A. Warshel and S. Russell, J. Am. Chem. Soc. **108**, 6569 (1986).
[93] J.-K. Hwang, G. King, S. Creighton, and A. Warshel, J. Am. Chem. Soc. **110**, 5297 (1988).
[94] A. Warshel and Z.T. Chu, J. Chem. Phys. **93**, 4003 (1990).
[95] J.-K. Hwang, S. Creighton, G. King, D. Whitney, and A. Warshel, J. Chem. Phys. **89**, 859 (1988).
[96] J. Aqvist and A. Warshel, Chem. Rev. **93**, 2523 (1993).
[97] P. J. Kuntz, in *The Diatomics-in-Molecules Method and the Chemical Bond*, edited by Z. B. Maksic (Springer-Verlag, New York, 1990).
[98] J.C. Tully, in *Semiempirical Methods of Electronic Structure Calculation, Part A: Techniques*, edited by G.A. Segal (Plenum, New York, 1977).
[99] I. Last and T.F. George, J. Chem. Phys. **87**, 1183 (1987).
[100] L.M. Julien and W.B. Preston, J. Phys. Chem. **72**, 3059 (1968).
[101] M. Saute and M. Aubert-Frecon, J. Chem. Phys. **77**, 5639 (1982).
[102] T.Y. Chang, Rev. Mod. Phys. **39**, 911 (1967).
[103] S. Ya. Umanskij and E.E. Nikitin, Theor. Chim. Acta **13**, 91 (1969).
[104] P. Luc, J. Mol. Spectrosc. **80**, 41 (1980).
[105] S. Churrasy, F. Martin, R. Bacis, J. Verges, and R. W. Field, J. Chem. Phys. **75**, 4863 (1981).
[106] J. Tellinghuisen, J. Chem. Phys. **82**, 4012 (1985).
[107] K. S. Viswanathan, A. Sur, and J. Tellinghuisen, J. Mol. Spectrosc. **86**, 393 (1981).
[108] J. Tellinghuisen, J. Mol. Spectrosc. **94**, 231 (1982).
[109] J. Tellinghuisen, J. Mol. Spectrosc. **101**, 285 (1983).
[110] Le Roy, J. Chem. Phys. **52**, 2683 (1970).
[111] E. P. Gordeev, S. Ya. Umansky, and A. I Voronin, Chem. Phys. Lett. **23**, 524 (1973).
[112] R. Mulliken, J. Chem. Phys. **55**, 288 (1971).
[113] P. Casavecchia, G. He, R. K. Sparks, and Y. T. Lee, J. Chem. Phys. **77**, 1878 (1982).
[114] C. H. Becker, P. Casavecchia, and Y. T. Lee, J. Chem. Phys. **70**, 5477 (1979).
[115] A.A. Buchachenko and N.F. Stepanov, J. Chem. Phys. **104**, 9913 (1996).
[116] L. Xiao and D.F. Coker, J. Chem. Phys. **100**, 8464 (1994).
[117] V.S. Batista and D.F. Coker (in preparation).
[118] M.L. Burke and W. Klemperer, J. Chem. Phys. **98**, 1797 (1993).
[119] J. Franck and E. Rabinowitch, Trans. Faraday Soc. **30**, 120 (1934).
[120] L.F. Meadows and R.M. Noyes, J. Am. Chem. Soc. **82**, 1872 (1960).
[121] T.J. Chuang, G.W. Hoffman, and K.B. Eisenthal, Chem. Phys. Lett. **25**, 201 (1974).
[122] J.I. Steinfeld, J. Chem. Phys. **44**, 2740 (1966).
[123] J. Xu, N. Schwentner, S. Hennig, and M. Chergui, J. Chim. Phys. **92**, 541 (1995).
[124] J. Xu, N. Schwentner, and M. Chergui, J. Chem. Phys., **101**, 7381 (1994).
[125] J. Tellinghuisen, J. Chem. Phys. **82**, 4012 (1985).
[126] P.S. Dardi and J.S. Dahler, J. Chem. Phys. **98**, 363 (1993).
[127] S.Y. Lee and E.J. Heller, J. Chem. Phys. **71**, 4777 (1979).